AIAA JOURNAL
Vol. 44, No. 10, October 2006

High-Order Unstructured Essentially Nonoscillatory and Weighted Essentially Nonoscillatory Schemes for Aerodynamic Flows

William R. Wolf*
Instituto Tecnológico de Aeronáutica, Centro Técnico Aerospacial, 12228-900 São José dos Campos, São Paulo, Brazil
and
João Luiz F. Azevedo†
Instituto de Aeronáutica e Espaço, Centro Técnico Aerospacial, 12228-904 São José dos Campos, São Paulo, Brazil

DOI: 10.2514/1.19373

In the present work, essentially nonoscillatory schemes and weighted essentially nonoscillatory schemes are implemented in a cell centered finite volume context on unstructured meshes. The two-dimensional Euler equations are considered to represent the flows of interest. The essentially nonoscillatory and weighted essentially nonoscillatory schemes have been developed with the purpose of accurately capturing discontinuities appearing in problems governed by hyperbolic conservation laws. In the aerodynamic studies of interest in the paper, these discontinuities are mainly represented by shock waves. The entire reconstruction process of essentially nonoscillatory and weighted essentially nonoscillatory schemes is described in detail for any order of accuracy with an emphasis on the implementation of second-order and third-order schemes. A flux-difference splitting method and a flux-vector splitting method are tested and compared. The code developed also features an agglomeration multigrid procedure for convergence acceleration, and an adaptive mesh refinement tool. Applications for aerodynamic flows are performed to assess the capability implemented against data available in the literature.

Nomenclature

C	=	convective operator
c	=	speed of sound
E, F	=	flux vectors in the (x, y) Cartesian directions, respectively
e	=	total energy per unit of volume
G	=	Gaussian point
H	=	total enthalpy
h	=	mesh width
M	=	Mach number
$\boldsymbol{n}$	=	unit normal vector to the surface, positive outward
OI	=	oscillation indicator
p	=	pressure
$\boldsymbol{Q}$	=	vector of conserved properties
S	=	surface of the control volume
t	=	time
u, v	=	velocity components in the (x, y) Cartesian directions, respectively
V	=	control volume
w	=	Gaussian weight
z	=	end point of the edge
γ	=	ratio of specific heats
ρ	=	density
Γ	=	edge of the control volume
ω	=	weighted essentially nonoscillatory weight

Subscripts

i	=	ith volume
ng	=	ngth neighbor of the ith volume

Superscript

n	=	nth iteration

Presented as Paper 5115 at the 17th AIAA Computational Fluid Dynamics Conference, Toronto, Ontario, Canada, 6–9 June 2005; received 9 August 2005; revision received 19 February 2006; accepted for publication 6 May 2006.

*Graduate Student, Department of Computer & Electronic Engineering; e-mail wolf@ita.br.

†Currently Director for Space Transportation and Licensing, Brazilian Space Agency; e-mail azevedo@iae.cta.br. Associate Fellow AIAA.

I. Introduction

THE motivation for the present work is the need for accurate simulations of high Mach number aerodynamic flows with strong discontinuities. In recent years, several efforts have been made by the computational fluid dynamics (CFD) group of Instituto de Aeronáutica e Espaço [1–3] for the development of computational tools which are capable of accurately capturing discontinuities such as the shock waves appearing in the aerodynamic flows of interest. Some upwind schemes such as the van Leer flux-vector splitting (FVS) scheme [4], the Liou AUSM$^+$ FVS scheme [5], and the Roe flux-difference splitting (FDS) scheme [6] were implemented and tested for second-order accuracy considering a TVD–MUSCL reconstruction [7]. However, [3] shows that nominally second-order schemes presented results with an order of accuracy smaller than the expected in the solutions for unstructured grids. Aside from this fact, it is well known that total variation diminishing (TVD) schemes have their order of accuracy reduced to first order in the presence of shocks due to the effect of limiters.

This observation initiated the development and implementation of essentially nonoscillatory (ENO) schemes, introduced by Harten et al. [8], in which oscillations up to the order of the truncation error are allowed to overcome the drawbacks and limitations of TVD schemes. Subsequent to the development of ENO schemes, the weighted essentially nonoscillatory (WENO) schemes were introduced by Liu et al. [9] with the purpose of presenting better convergence rate for stationary cases, better smoothing for the flux vectors, and better accuracy using the same stencils as the ENO schemes.

In this work, the ENO schemes and the WENO schemes are implemented in a cell centered finite volume context for unstructured meshes. The two-dimensional (2-D) Euler equations are considered to represent the flows of interest. The ENO and WENO schemes have been developed with the purpose of accurately capturing discontinuities appearing in problems governed by hyperbolic conservation laws. In the aerodynamic studies of interest in the present paper, these discontinuities are mainly represented by shock waves. The entire reconstruction process of ENO and WENO schemes is described in detail for linear and quadratic polynomials and, hence, for second and third-order accuracy of the numerical schemes, with extension to higher orders. Applications to aerodynamic flows are presented showing the capability implemented and the behavior of the various schemes. For the ENO schemes, interpolation polynomials of one order less than the order of accuracy expected in the solution are computed and these polynomials are used to reconstruct a good approximation to the values of the conserved variables within the cells. These polynomials interpolate primitive variable values in Gauss quadrature points using stencils determined by a von Neumann neighborhood [10]. The control volume moments and the mean values of primitive variables in the cells are used to compute the polynomial coefficients and, hence, one can compute the oscillation indicator of the polynomials and select the smoothest among them through the values of these coefficients.

Whereas the ENO schemes use the smoothest polynomial, the WENO schemes use all ENO computed polynomials for the stencils and, therefore, they construct one polynomial only. Nonnegative weights, which must add up to one, are computed for every polynomial through oscillation indicators and the WENO polynomial is constructed by the sum of all the ENO polynomials multiplied by the respective weights [9,11]. The weights attributed to the polynomials can be of the order of accuracy desired in the solution if these polynomials are in the discontinuous regions of the mesh or they can be of order one if the polynomials are in the smooth regions of the flow. Classical CFD applications such as shock tube problems, the flow past a wedge, the Ringleb flow [27], the flow in a channel with a forward-facing step, the transonic flow over a NACA 0012 airfoil, and the transonic flow over a RAE 2822 airfoil are presented with the aim of comparing the behavior of the proposed methods. Such an assessment of the methods implemented is achieved through the comparison of the present numerical results with data available in the literature.

II. Theoretical Formulation

A. Governing Equations

In the present work, the 2-D Euler equations are solved in their integral form as

$$\frac{\partial}{\partial t}\int_V \boldsymbol{Q}\,\mathrm{d}V + \int_V (\nabla\cdot\boldsymbol{P})\,\mathrm{d}V = 0 \tag{1}$$

where $\boldsymbol{P} = \boldsymbol{E}\hat{\imath} + \boldsymbol{F}\hat{\jmath}$. The application of the divergence theorem to Eq. (1) yields

$$\frac{\partial}{\partial t}\int_V \boldsymbol{Q}\,\mathrm{d}V + \int_S (\boldsymbol{P}\cdot\boldsymbol{n})\,\mathrm{d}S = 0 \tag{2}$$

The vector of conserved variables $\boldsymbol{Q}$ and the convective flux vectors $\boldsymbol{E}$ and $\boldsymbol{F}$ are given by

$$\boldsymbol{Q} = \begin{Bmatrix} \rho \\ \rho u \\ \rho v \\ e \end{Bmatrix}, \qquad \boldsymbol{E} = \begin{Bmatrix} \rho u \\ \rho u^2 + p \\ \rho uv \\ (e+p)u \end{Bmatrix}, \qquad \boldsymbol{F} = \begin{Bmatrix} \rho v \\ \rho uv \\ \rho v^2 + p \\ (e+p)v \end{Bmatrix} \tag{3}$$

The system is closed by the equation of state for a perfect gas

$$p = (\gamma - 1)\left[e - \frac{1}{2}\rho(u^2 + v^2)\right] \tag{4}$$

where the ratio of specific heats γ was chosen as 1.4 for all the computations in this work.

Equation (2) discretized in a cell centered finite volume context can be rewritten for the ith control volume as

$$\frac{\partial \boldsymbol{Q}_i}{\partial t} = -\frac{1}{V_i}\int_{S_i} (\boldsymbol{P}\cdot\boldsymbol{n})\,\mathrm{d}S \tag{5}$$

where $\boldsymbol{Q}_i$ is the mean value of $\boldsymbol{Q}$ at time t over the ith control volume V_i.

B. Spatial Discretization

The spatial discretization is concerned with finding a discrete approximation to the integral on the right-hand side of Eq. (5). The control volumes considered in this work are triangles and quadrilaterals and their boundaries can be decomposed into a finite number of line segments Γ_j. One should observe that the control volumes could be composed by any type of polygon, because the really important aspect is that its bounding contour could be decomposed into a finite number of line segments. Hence, it is possible to write

$$S_i = \bigcup \Gamma_j \tag{6}$$

Thus, the boundary integral from Eq. (5) can be decomposed into

$$C(\boldsymbol{Q}_i) \equiv \int_{S_i} (\boldsymbol{P}\cdot\boldsymbol{n})\,\mathrm{d}S = \sum_j \int_{\Gamma_j} (\boldsymbol{P}\cdot\boldsymbol{n})\,\mathrm{d}S \tag{7}$$

and, as $\boldsymbol{n}$ is constant on each line segment Γ_j the right side of Eq. (7) is discretized using N-point Gaussian integration formulas with degree $2N-1$ and order of accuracy $2N$. Using such integration formulas, one obtains the following approximation

$$\int_{S_i} (\boldsymbol{P}\cdot\boldsymbol{n})\,\mathrm{d}S \approx \sum_j |\Gamma_j| \sum_{\ell=1}^{N} w_\ell \boldsymbol{P}[\boldsymbol{Q}(G_\ell), t]\cdot\boldsymbol{n} \tag{8}$$

where G_ℓ and w_ℓ are, respectively, the Gaussian points and the weights on the Γ_j line segment.

For the second-order schemes, one Gaussian point is used in the integration. Given the coordinates of the end points z_1 and z_2, one can obtain the Gaussian point as the middle point of the segment connecting the two end points $G_1 = (z_1 + z_2)/2$. For this case the weight w_1 is chosen as $w_1 = 1$. For the third-order schemes, two Gaussian points are necessary along each line segment. Their values are given by

$$\begin{aligned} G_1 &= \frac{\sqrt{3}+1}{2\sqrt{3}} z_1 + \left(1 - \frac{\sqrt{3}+1}{2\sqrt{3}}\right) z_2 \quad \text{and} \\ G_2 &= \frac{\sqrt{3}+1}{2\sqrt{3}} z_2 + \left(1 - \frac{\sqrt{3}+1}{2\sqrt{3}}\right) z_1 \end{aligned} \tag{9}$$

and the respective weights w_1 and w_2 are chosen as $w_1 = w_2 = 1/2$.

Using the method described in the preceding example, one can compute values of $\boldsymbol{Q}_i$ in some instant t and then, from these mean values, one can reconstruct polynomials that represent the primitive variables ρ, u, v, and p. Finally, it is possible to compute values of the conserved variables in the Gaussian points. Because of the discontinuity of the reconstructed values of the conserved variables over the cell boundaries, one must use a numerical flux function to approximate the flux values on the cell boundaries. In this work, the authors have used the Roe flux-difference splitting method [6] and the Liou AUSM+ flux-vector splitting method [5] to compute such

approximations. Hence, for the Roe scheme, the flux evaluation on the right-hand side of Eq. (8) is computed as

$$\begin{aligned}\boldsymbol{P}[\boldsymbol{Q}_j(G_\ell),t]\cdot\boldsymbol{n} &\approx \mathcal{P}[\boldsymbol{Q}_i(G_\ell),\boldsymbol{Q}_{ng}(G_\ell),t;\,\boldsymbol{n}]\\ &=\frac{1}{2}\{\boldsymbol{P}[\boldsymbol{Q}_i(G_\ell)]+\boldsymbol{P}[\boldsymbol{Q}_{ng}(G_\ell)]\}\cdot\boldsymbol{n}\\ &-\frac{1}{2}|A[\boldsymbol{Q}_i(G_\ell),\boldsymbol{Q}_{ng}(G_\ell),t;\,\boldsymbol{n}]|[\boldsymbol{Q}_{ng}(G_\ell)-\boldsymbol{Q}_i(G_\ell)]\end{aligned}\tag{10}$$

In Eq. (10), the $|A|$ matrix is a positive semidefinite matrix formed from the flux Jacobian matrix in the sense defined by Roe [6]. In the same equation, $\boldsymbol{Q}_i(G_\ell)$ is the vector of conserved variables computed at the quadrature point G_ℓ using the polynomial reconstruction associated to the ith control volume. Similarly, $\boldsymbol{Q}_{ng}(G_\ell)$ is the vector of conserved variables computed at the same quadrature point G_ℓ, but using the polynomial reconstruction associated with the ngth control volume. Here, it is being assumed that ng represents the neighbor of the ith control volume, which shares the Γ_j line segment with the ith cell.

The numerical flux of the scheme can be obtained by evaluating the last term on the right of Eq. (10) as

$$\begin{aligned}&|A[\boldsymbol{Q}_i(G_\ell),\boldsymbol{Q}_{ng}(G_\ell),t;\boldsymbol{n}]|[\boldsymbol{Q}_{ng}(G_\ell,t)-\boldsymbol{Q}_i(G_\ell,t)]\\ &\quad=\sum_m|\lambda_m|\partial w_m r^{(m)}\end{aligned}\tag{11}$$

where λ_m are the eigenvalues of the flux Jacobian matrix, $r^{(m)}$ are the associated right eigenvectors, and ∂w_m are the corresponding characteristic variables. The first step in the calculation of the Roe [6] numerical flux is concerned with the evaluation of the properties averages defined by Roe as

$$\begin{aligned}\tilde\rho &= \sqrt{\rho_i\rho_{ng}},\\ \tilde u &= \frac{u_i\sqrt{\rho_i}+u_{ng}\sqrt{\rho_{ng}}}{\sqrt{\rho_i}+\sqrt{\rho_{ng}}},\\ \tilde v &= \frac{v_i\sqrt{\rho_i}+v_{ng}\sqrt{\rho_{ng}}}{\sqrt{\rho_i}+\sqrt{\rho_{ng}}},\\ \tilde H &= \frac{H_i\sqrt{\rho_i}+H_{ng}\sqrt{\rho_{ng}}}{\sqrt{\rho_i}+\sqrt{\rho_{ng}}}\end{aligned}\tag{12}$$

One should observe that, in the original reference [6], the averaged density term is not cited by the author. However, the present implementation considers this term as suggested by Hirsch [12]. The normal velocity is then computed using the averaged values of the Cartesian velocities as $\hat V=\tilde u n_x+\tilde v n_y$, where n_x and n_y are the direction cosines in the x and y Cartesian directions, respectively. The average speed of sound $\tilde c$ is subsequently computed as

$$\tilde c^{\,2}=(\gamma-1)\left(\tilde H-\frac{\tilde u^2+\tilde v^2}{2}\right)\tag{13}$$

and the eigenvalues of the A matrix and the associated right eigenvectors are obtained by the following relations

$$\begin{aligned}\lambda_1&=\hat V,\\ \lambda_2&=\hat V,\\ \lambda_3&=\hat V+\tilde c_n,\\ \lambda_4&=\hat V-\tilde c_n\end{aligned}\tag{14}$$

$$\begin{aligned}r^{(1)}&=\begin{Bmatrix}1\\ \tilde u\\ \tilde v\\ \frac{\tilde u^2+\tilde v^2}{2}\end{Bmatrix},\\ r^{(2)}&=\tilde\rho\begin{Bmatrix}0\\ n_y\\ -n_x\\ \tilde u n_y-\tilde v n_x\end{Bmatrix},\\ r^{(3)}&=\frac{\tilde\rho}{2\tilde c}\begin{Bmatrix}1\\ \tilde u+\tilde c n_x\\ \tilde v+\tilde c n_y\\ \tilde H+\tilde c\,\hat V\end{Bmatrix},\\ r^{(4)}&=\frac{\tilde\rho}{2\tilde c}\begin{Bmatrix}1\\ \tilde u-\tilde c n_x\\ \tilde v-\tilde c n_y\\ \tilde H-\tilde c\,\hat V\end{Bmatrix}\end{aligned}\tag{15}$$

Finally, the characteristic variables are defined as

$$\begin{aligned}\partial w_1&=\partial\rho-\frac{\partial p}{\tilde c^2},\\ \partial w_2&=n_y\partial u-n_x\partial v,\\ \partial w_3&=n_x\partial u+n_y\partial v+\frac{\partial p}{\tilde c\,\tilde\rho},\\ \partial w_4&=-n_x\partial u-n_y\partial v+\frac{\partial p}{\tilde c\,\tilde\rho}\end{aligned}\tag{16}$$

where $\partial(\,)=(\,)_{ng}-(\,)_i$.

For the Liou scheme, the convective operator can be expressed as a sum of the convective and pressure terms [5]. The flux vectors can be written as

$$\begin{aligned}\boldsymbol{E}&=u\Phi+p_x=M_x c\Phi+p_x,\\ \boldsymbol{F}&=v\Phi+p_y=M_y c\Phi+p_y\end{aligned}\tag{17}$$

where the Φ, p_x, and p_y vectors are defined as

$$\Phi=\begin{Bmatrix}\rho\\ \rho u\\ \rho v\\ \rho H\end{Bmatrix},\qquad p_x=\begin{Bmatrix}0\\ p\\ 0\\ 0\end{Bmatrix},\qquad p_y=\begin{Bmatrix}0\\ 0\\ p\\ 0\end{Bmatrix}\tag{18}$$

In the preceding expressions, p is the pressure, H is the total specific enthalpy, $M_x=u/c$, and $M_y=v/c$. One can finally evaluate the flux as

$$\begin{aligned}\boldsymbol{P}[\boldsymbol{Q}_j(G_\ell),t]\cdot\boldsymbol{n}&\approx\mathcal{P}[\boldsymbol{Q}_i(G_\ell),Q_{ng}(G_\ell),t;\boldsymbol{n}]\\ &=\frac{1}{2}M_{i,ng}c_{i,ng}(\Phi_i+\Phi_{ng})-\frac{1}{2}|M_{i,ng}|c_{i,ng}(\Phi_{ng}-\Phi_i)\\ &+\{0\quad p_{i,ng}n_x\quad p_{i,ng}n_y\quad 0\}^T\end{aligned}\tag{19}$$

where $M_{i,ng}$ is the interface Mach number defined according to [5] as $M_{i,ng}=M_i^+ + M_{ng}^-$ with $M_i^+=M^+(M_i)$ and $M_{ng}^-=M^-(M_{ng})$. The split Mach numbers are defined as

$$M_i^+=\begin{cases}\frac{1}{2}(M_i+|M_i|), & \text{if } |M_i|\geq 1\\ M_\beta^+(M_i), & \text{otherwise}\end{cases}\tag{20}$$

and, similarly

$$M_{ng}^{-} = \begin{cases} \frac{1}{2}(M_{ng} - |M_{ng}|), & \text{if } |M_{ng}| \geq 1 \\ M_{\beta}^{-}(M_{ng}), & \text{otherwise} \end{cases} \tag{21}$$

The $M_{\beta}^{\pm}$ terms can be written as

$$M_{\beta}^{\pm}(M) = \pm\frac{1}{4}(M \pm 1)^2 \pm \beta(M^2 - 1)^2 \tag{22}$$

This work used $\beta = 1/8$, as suggested in [13]. Moreover, to achieve a unique splitting in Liou's [5] sense, the ith and ngth Mach numbers are defined as

$$M_i = \frac{\tilde{V}_i}{c_{i,ng}} \quad \text{and} \quad M_{ng} = \frac{\tilde{V}_{ng}}{c_{i,ng}} \tag{23}$$

where $\tilde{V}_i = u_i n_x + v_i n_y$ and $\tilde{V}_{ng} = u_{ng} n_x + v_{ng} n_y$. The corresponding speed of sound $c_{i,ng}$, at the interface, is given by $c_{i,ng} = \min(c_i, c_{ng})$, where

$$c_i = c_i^* \min\left(1, \frac{c_i^*}{|\tilde{V}_i|}\right) \tag{24}$$

$$c_i^* = \sqrt{\frac{2(\gamma - 1)}{\gamma + 1} H_i} \tag{25}$$

and a similar definition for c_{ng} is considered. The pressure $p_{i,ng}$ at the interface between the ith and ngth cells is given by $p_{i,ng} = p_i^{+} p_i + p_{ng}^{-} p_{ng}$. The split pressures, still following the expressions in [13], can be written as

$$p_i^{+} = \begin{cases} \frac{1}{2}[1 + \text{sign}(M_i)], & \text{if } |M_i| \geq 1 \\ p_{\alpha}^{+}(M_i), & \text{otherwise} \end{cases} \tag{26}$$

and, similarly

$$p_{ng}^{-} = \begin{cases} \frac{1}{2}[1 - \text{sign}(M_{ng})], & \text{if } |M_{ng}| \geq 1 \\ p_{\alpha}^{-}(M_{ng}), & \text{otherwise} \end{cases} \tag{27}$$

Finally, the $p_{\alpha}^{\pm}$ terms can be written as

$$p_{\alpha}^{\pm}(M) = \frac{1}{4}(M \pm 1)^2(2 \mp M) \pm \alpha M(M^2 - 1)^2 \tag{28}$$

with the term $\alpha = 3/16$, as suggested in [13].

C. Temporal Discretization

The temporal discretization is concerned with solving a system of ordinary differential equations, hence, an ODE problem which can be written as

$$\frac{\mathrm{d}\boldsymbol{Q}_i}{\mathrm{d}t} = -\frac{1}{V_i} C(\boldsymbol{Q}_i) \tag{29}$$

In this work, two different, fully explicit second-order accurate Runge–Kutta schemes were used to advance the solution of the governing equations in time, for the spatially second-order schemes, with the purpose of comparing the solutions and the stability of the schemes with respect to the CFL number. Both schemes are second-order accurate, where the first is a five-stage Runge–Kutta time-stepping scheme [14] and the second is a two-stage TVD Runge–Kutta time-stepping scheme [15]. The schemes can be written as

$$\begin{aligned}
\boldsymbol{Q}_i^{(0)} &= \boldsymbol{Q}_i^{n} \\
\boldsymbol{Q}_i^{(1)} &= \boldsymbol{Q}_i^{(0)} - \alpha_1 \frac{\Delta t_i}{V_i} C(\boldsymbol{Q}_i^{(0)}) \\
\boldsymbol{Q}_i^{(2)} &= \boldsymbol{Q}_i^{(0)} - \alpha_2 \frac{\Delta t_i}{V_i} C(\boldsymbol{Q}_i^{(1)}) \\
&\vdots \quad \vdots \\
\boldsymbol{Q}_i^{(5)} &= \boldsymbol{Q}_i^{(0)} - \alpha_5 \frac{\Delta t_i}{V_i} C(\boldsymbol{Q}_i^{(4)}) \\
\boldsymbol{Q}_i^{n+1} &= \boldsymbol{Q}_i^{(5)}
\end{aligned} \tag{30}$$

for the five-stage scheme, and as

$$\begin{aligned}
\boldsymbol{Q}_i^{(0)} &= \boldsymbol{Q}_i^{n} \\
\boldsymbol{Q}_i^{(1)} &= \boldsymbol{Q}_i^{(0)} - \alpha_1 \frac{\Delta t_i}{V_i} C(\boldsymbol{Q}_i^{(0)}) \\
\boldsymbol{Q}_i^{(2)} &= \boldsymbol{Q}_i^{(0)} - \alpha_2 \frac{\Delta t_i}{V_i} C(\boldsymbol{Q}_i^{(0)}) - \alpha_3 \frac{\Delta t_i}{V_i} C(\boldsymbol{Q}_i^{(1)}) \\
\boldsymbol{Q}_i^{n+1} &= \boldsymbol{Q}_i^{(2)}
\end{aligned} \tag{31}$$

for the two-stage scheme. The superscripts n and $n + 1$ denote, respectively, the values of the properties at the beginning and at the end of the nth time step. In Eq. (30), as suggested in [14], the α coefficients are $\alpha_1 = 1/4$, $\alpha_2 = 1/6$, $\alpha_3 = 3/8$, $\alpha_4 = 1/2$ and $\alpha_5 = 1$. In Eq. (31) the α coefficients are $\alpha_1 = 1/4$, $\alpha_2 = 1/2$, and $\alpha_3 = 1/2$, as suggested in [15]. For the spatially third-order scheme, a fully explicit third-order accurate TVD Runge–Kutta scheme [15] was used in the present work and it can be written as

$$\begin{aligned}
\boldsymbol{Q}_i^{(0)} &= \boldsymbol{Q}_i^{n} \\
\boldsymbol{Q}_i^{(1)} &= \boldsymbol{Q}_i^{(0)} - \alpha_1 \frac{\Delta t_i}{V_i} C(\boldsymbol{Q}_i^{(0)}) \\
\boldsymbol{Q}_i^{(2)} &= \boldsymbol{Q}_i^{(0)} - \alpha_2 \frac{\Delta t_i}{V_i} C(\boldsymbol{Q}_i^{(0)}) - \alpha_3 \frac{\Delta t_i}{V_i} C(\boldsymbol{Q}_i^{(1)}) \\
\boldsymbol{Q}_i^{(3)} &= \boldsymbol{Q}_i^{(0)} - \alpha_4 \frac{\Delta t_i}{V_i} C(\boldsymbol{Q}_i^{(0)}) - \alpha_5 \frac{\Delta t_i}{V_i} C(\boldsymbol{Q}_i^{(1)}) - \alpha_6 \frac{\Delta t_i}{V_i} C(\boldsymbol{Q}_i^{(2)}) \\
\boldsymbol{Q}_i^{n+1} &= \boldsymbol{Q}_i^{(3)}
\end{aligned} \tag{32}$$

where the α coefficients are $\alpha_1 = 1$, $\alpha_2 = 1/4$, $\alpha_3 = 1/4$, $\alpha_4 = 1/6$, $\alpha_5 = 1/6$, and $\alpha_6 = 2/3$, as suggested in [15].

III. ENO and WENO Reconstructions

A. General Considerations and Oscillation Indicators

The reconstruction procedure of the ENO schemes is based on the approximation of mean values of the primitive variables for each cell in the mesh by polynomials of one order less than the spatial order of accuracy expected. For the construction of polynomials of ηth order, one must use $N(\eta)$ cells, where $N(\eta) = (\eta + 1)(\eta + 2)/2$. The first step in obtaining the polynomial reconstruction for each cell is to define the possible set of cells, called a stencil, that will be used. In the finite volume cell centered scheme, the stencils can be selected in a von Neumann neighborhood for a linear polynomial reconstruction (second-order accuracy). This approach can be extended to higher orders through the use of von Neumann neighborhoods of the primary neighbors already selected for the second-order reconstruction. In the present work, the cells are triangles or quadrilaterals and the $p(x, y)$ polynomials can then be calculated as

$$p(x, y) = \sum_{|\beta| \leq \eta} r_{\beta_1 \beta_2} (x - x_c)^{\beta_1} (y - y_c)^{\beta_2} \tag{33}$$

where $|\beta| = \beta_1 + \beta_2$, with $\beta_i \in \{0, 1, 2, \ldots\}$, x_c and y_c are the Cartesian coordinates of the barycenter of the control volumes, and

$r_{\beta_1\beta_2}$ are unknown coefficients which represent approximations to the derivatives of the primitive variables.

By imposing that the integration of $p(x, y)$ along each cell of the stencil returns the mean value for the corresponding primitive variable in that cell, one can write a linear system $[R]\{r\} = \{\bar{u}\}$ of $N(\eta)$ equations for the $N(\eta)$ unknowns, $r_{\beta_1\beta_2}$. Here, $[R]$ is the matrix of control volume moments, as in Gooch [16], computed using the scaling technique proposed by Friedrich [11] to circumvent a poorly conditioned matrix. Moreover, $\{r\}$ is the vector of unknown coefficients that must be found and $\{\bar{u}\}$ is the vector composed by the mean values for each primitive variable. The stencil is considered admissible if the $[R]$ matrix is invertible. There are other approaches for the calculation of the polynomials, as the one proposed by Abgrall [17], which uses interpolation through barycentric coordinates, or the one proposed by Hu and Shu [18], which is based in reconstructing high-order polynomials using only linear polynomials. These alternate approaches, however, are beyond the scope of the present paper.

The control volume moments that compose the $[R]$ matrix are defined as

$$\overline{x^{\varphi} y^{\zeta}} \equiv \frac{1}{V_i} \int_{V_i} (x - x_c)^{\varphi} (y - y_c)^{\zeta} \, \mathrm{d}V \tag{34}$$

and are evaluated using Gauss quadrature formulas following the same procedure as the one used in the flux computation. To avoid computing moments of each control volume for all the stencils, one can replace the terms $(x - x_c)$ and $(y - y_c)$ with $(x - x_{cj}) + (x_{cj} - x_c)$ and $(y - y_{cj}) + (y_{cj} - y_c)$, respectively. The new terms appearing in the equations are simply the split between the distances of the centroids of the V_j and V_i control volumes plus the initial terms evaluated using the centroids of the V_j volume instead of the centroids of the V_i volume. Finally, the control volume moments are calculated, saving computational cost and memory storage, by the following general form

$$\begin{aligned} \overline{x^{\varphi} y^{\zeta}}_{ij} &\equiv \frac{1}{V_i} \int_{V_i} [(x - x_{cj}) + (x_{cj} - x_c)]^{\varphi} [(y - y_{cj}) + (y_{cj} - y_c)]^{\zeta} \, \mathrm{d}V \\ &= \sum_{\chi=0}^{\zeta} \sum_{\xi=0}^{\varphi} \binom{\zeta}{\chi} \binom{\varphi}{\xi} (x - x_{cj})^{\xi} (y - y_{cj})^{\chi} \overline{x^{\varphi-\xi} y^{\zeta-\chi}} \end{aligned} \tag{35}$$

After the polynomial reconstruction is performed for each stencil, the next step is to verify which polynomial is the least oscillatory to use in the ENO scheme. The oscillation is computed using some indicator that assesses the smoothness of $p(x, y)$. Abgrall [17] proposed the oscillation indicator defined as

$$\mathrm{OI}_{Ab}[p(x, y)] = \sum_{|\beta|=\eta} |r_{\beta_1\beta_2}| \tag{36}$$

which is the absolute value of the summation of the highest degree polynomial coefficients. Harten and Chakravarthy [19] proposed the indicator given by

$$\mathrm{OI}_{HC}[p(x, y)] = \sqrt{\sum_{\tau=1}^{\eta} \sum_{|\beta|=\tau} r_{\beta_1\beta_2}^2} \tag{37}$$

Jiang and Shu [20] proposed an indicator, which was later modified by Friedrich [11], that can be expressed as

$$\mathrm{OI}_{JS}[p(x, y)] = \left[\sum_{1 \le |\beta| \le \eta} \int_{V_i} h^{2|\beta|-4} \left(\frac{\partial^{|\beta|} p(x, y)}{\partial x^{\beta 1} \partial y^{\beta 2}} \right)^2 \mathrm{d}x \, \mathrm{d}y \right]^{\frac{1}{2}} \tag{38}$$

In the present computations, the diameter of the inscribed circle was considered as the mesh width, h. The preceding three oscillation indicators cited were tested and compared in the present work.

Differently from the ENO schemes, the WENO schemes use all the calculated polynomials. These polynomials are added together through the use of weights, which are computed for each one of the polynomials as proportional to its respective oscillation indicator. The main idea in the WENO reconstruction is to attribute the computed weights for each polynomial with the aim of reconstructing a new polynomial as

$$p(x, y) = \sum_{k=1}^{m} \omega_k p_k(x, y)$$

The weights are of order one in the smooth regions of the flow and are of the order of the desired accuracy in the solution in the regions with discontinuities. The weights can be computed as

$$\omega_k = \frac{\{\epsilon + \mathrm{OI}[p_k(x, y)]\}^{-\theta}}{\sum_{k'=1}^{m} \{\epsilon + \mathrm{OI}[p_{k'}(x, y)]\}^{-\theta}} \tag{39}$$

where ϵ is a small real number used to avoid division by zero and θ is a positive integer. The WENO schemes have the property of being very smooth and stable in smooth regions of the flow, but this property is lost if θ is chosen too large. In that case, the scheme tends to behave like the ENO schemes. In the present work, the θ term is chosen as $\theta = 2$ because this yielded the best convergence rates in the results.

B. Second-Order Implementation

For the implementation of the second-order accurate schemes one must use three cells for the polynomial reconstructions. Hence, two unknown coefficients are computed for each polynomial through the solution of a two equation linear system composed by the control volume moments and the mean values of the primitive variables of the cells considered in the stencil. The first algorithm implemented uses only the primary neighbors of the main control volume. Therefore, if the cell is a triangle, it has three different neighbors, which allows the construction of three different polynomials. If the cell is a quadrilateral, it has four different neighbors and this allows the construction of six different polynomials. For this algorithm, one observes the appearance of oscillations in a small number of cells of the mesh, and these oscillations left the ENO and WENO schemes unstable. The second algorithm implemented uses the primary and secondary neighbors of the main control volume to construct the stencils. In this approach, the number of constructed polynomials is increased and the schemes became stable. However, for this algorithm, small oscillations have appeared in smooth regions of the flow when the selected ENO stencil was composed exclusively by primary neighbors. The third algorithm implemented considers the ideas found in Sonar [10], where the neighborhood is extended when compared to the first algorithm. However, the stencils are computed considering one primary neighbor and one secondary neighbor. As an example, for a triangle, one has six possible polynomials to choose from and, for a quadrilateral, one has 12 polynomials, if one imposes an additional restriction of only considering stencils in which the control volumes are contiguous. This algorithm does not present any oscillation in the solutions, keeps the schemes stable, and reduces the computational cost in comparison with the second algorithm implemented. In Fig. 1, one can see a typical neighborhood for the implementation of the first algorithm with a possible stencil (hatched

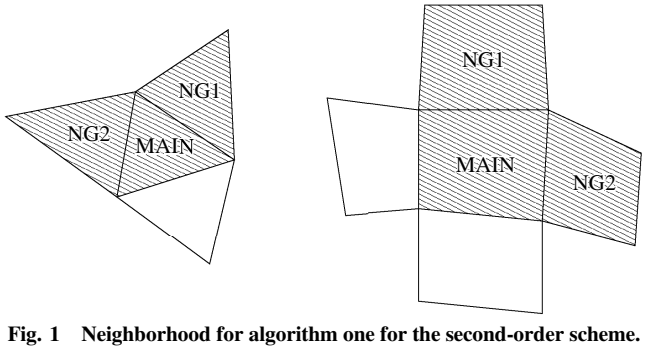

Fig. 1 Neighborhood for algorithm one for the second-order scheme.

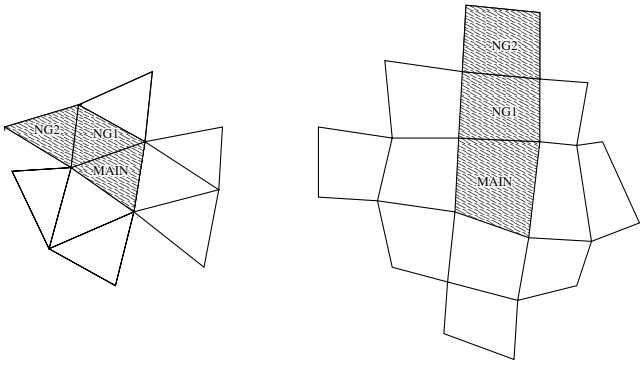

Fig. 2 Neighborhood for algorithms two and three for the second-order scheme.

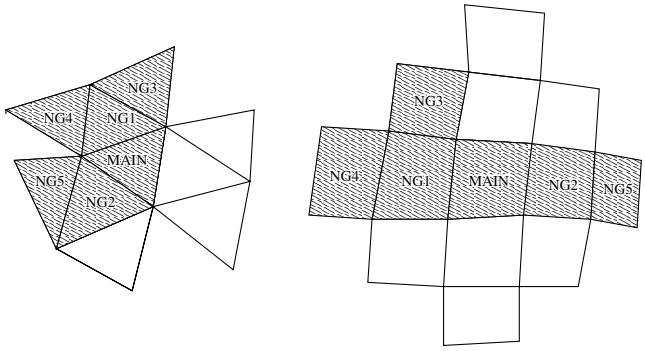

Fig. 3 Neighborhood for algorithms one and four for the third-order scheme.

volumes) for this algorithm and, in Fig. 2, one can see a typical neighborhood for the implementation of the second and third algorithms with a possible stencil (hatched volumes) for the third algorithm. The examples of neighborhoods presented here are for triangles and quadrilaterals. However, the geometry of the control volume is not relevant for the algorithms implemented. The control volumes can be formed by any type of polygon.

C. Third-Order Implementation

For the implementation of the third-order accurate schemes one must use six cells for the polynomial reconstructions. Five unknown coefficients are computed for each polynomial through the solution of a five equation linear system composed by the control volume moments and the mean values of the primitive variables of the cells considered in the stencil. Four different approaches were implemented in the present work for the ENO and WENO schemes with the aim of comparing the efficiency and accuracy of the approaches. The first algorithm implemented is based on the ideas proposed by Abgrall [17]. The first step consists in finding the stencil that presents the smoothest oscillation among the possible stencils for a linear reconstruction using only the primary neighbors of the main control volume. This algorithm uses this concept for both the ENO and WENO schemes for meshes composed by triangles and quadrilaterals. After the smoothest three-cell stencil is chosen, one must start the procedure for the third-order accuracy reconstruction. If the control volume is a triangle, one has a maximum of four secondary neighbors for the reconstruction and, therefore, four possibilities for stencil selection. However, if the control volume is a quadrilateral, one has a maximum of six secondary neighbors for the reconstruction and, therefore, 20 possibilities for stencil selection. In Fig. 3, one can see a typical neighborhood for the implementation of the first algorithm with the hatched volumes representing a possible stencil for this algorithm.

Although the case in which one has 20 stencils for the selection can occur, in most cases, one has five secondary neighbors for the reconstruction in quadrilaterals and then 10 possibilities for stencil selection. Such a situation happens because, when selecting the stencil with the primary neighbors, one has, in most cases, a stencil that is not centered as can be viewed in Fig. 4 for the control volumes labeled NG1 and NG2. In such case, one can see that there are five secondary neighbors (the control volumes labeled as "2ndNG"). In triangular control volumes, one can have the presence of three secondary neighbors for the reconstruction, which is the worst case for reconstruction in a triangular mesh. A case such this can be observed in Fig. 5, where the NG1 and NG2 hatched control volumes compose the smoothest stencil for a second-order reconstruction and the other hatched control volumes, NG3, NG4, and NG5 are the control volumes used for the third-order reconstruction. As one can see, this case allows the construction of only one stencil. If this stencil is in a discontinuous region of the flow, it will produce oscillations, and it will lead to a nonphysical solution. Hence, the procedure adopted to avoid the problem, where one has a stencil such as this in a discontinuous region of the flow, is to reduce the order of accuracy of the scheme in these cells.

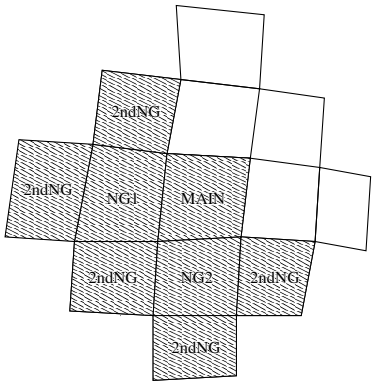

Fig. 4 Example of a reduced number of possible stencils for a quadrilateral mesh.

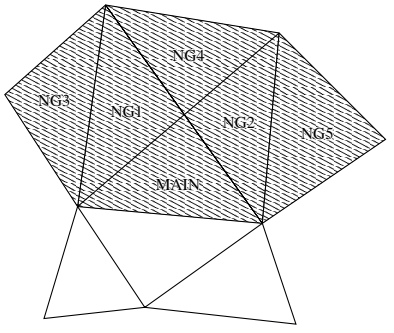

Fig. 5 Example of a reduced number of possible stencils for a triangular mesh.

The second algorithm implemented is based on the ideas of Harten and Chakravarthy [19] and Käser and Iske [21]. This algorithm is based on a sectorial search that keeps the number of possible stencils small. The approach consists in the search for stencils composed by cells that belong to the sectors. The basic idea for the implementation of the sectorial search is to include the von Neumann neighbors of the control volumes whose barycenters lie in one of the forward sectors or backward sectors of the main control volume, as defined in Käser and Iske [21]. Each forward sector is spanned by a corresponding edge pair of the control volume, such that the resulting sector contains the control volume. One can see the forward sectors for a triangle in Fig. 6. The backward sectors are defined by the midpoints of the edges of the control volume. Each backward sector has its origin at one midpoint and its two boundary edges pass through the other midpoints. One can see the backward sectors for a triangle in Fig. 7. This approach was implemented and tested only for triangles in the present code. The cost of these algorithm is very low compared with the others implemented in the present work, because the stencils are computed for each sector only in the first time iteration or when

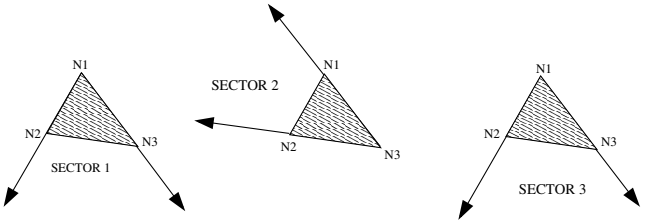

Fig. 6 Forward sectors for a triangle.

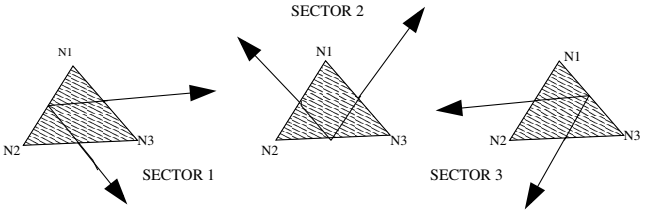

Fig. 7 Backward sectors for a triangle.

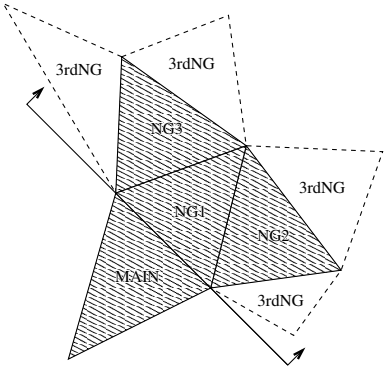

Fig. 8 Possible stencil for third-order accuracy scheme using algorithm three.

the adaptive refinement process is used. Furthermore, the maximum number of possible reconstructions spans six stencils for a triangle and this number is small when compared with the other approaches.

The third algorithm implemented works as an upwind stencil selection and it couples the ideas of both algorithms already discussed. The idea is to look across the edges of the main control volume. In other words, one must include the von Neumann neighbors of the control volumes as if they were in a sector bounded by the edges of the main control volume. One can see a stencil for this algorithm in Fig. 8. The volumes that belong to the other side of some edge of the main control volume are considered in the stencils if the flow has a direction opposite to that of the cells used in the stencil. Simply, one has the cells used to form the stencil in an upwind direction with regard to the flow direction. The first neighbor considered in the stencil is the primary neighbor that shares the edge with the main control volume (volume NG1 in Fig. 8). Following the natural sequence, one must select the secondary neighbors (volumes NG2 and NG3 in Fig. 8). These selected cells are fixed for this stencil and their neighbors, marked as 3rd NG, will be used to construct different stencils. This approach is simple to implement for any type of control volume. However, its computational cost is higher than that of the sectorial search and it is also more expensive than Abgrall's [17] ideas.

The fourth algorithm implemented is a variation of the first algorithm. The idea is to consider all the possible stencils for a third-order reconstruction instead of selecting the stencil that presents the smoothest oscillation for a second-order reconstruction. This algorithm is identical in the aspect of reconstruction when compared with the first algorithm. However, its cost is higher due to the larger number of possible third-order stencils. At least the reconstruction for a second-order stencil is avoided and this computational cost is saved.

The first algorithm has presented good results for most cases analyzed in the present work. As expected, the WENO schemes presented better results with respect to the convergence ratio and to the smoothness of the solution in comparison with the ENO schemes. As mentioned in the papers of Abgrall [17] and Harten and Chakravarthy [19], one has to reduce the order of accuracy in some cells to maintain the stability of the schemes for both the ENO and the WENO schemes. The technique used for the reduction of the order of accuracy is the same presented by Abgrall [17]. The second algorithm, which uses sectorial search, presented oscillations in the solution for simple test cases, as the supersonic flow over a wedge. For more complex test cases it has shown to be unstable, even with the reduction of the order of accuracy. The third algorithm presented a more diffusive solution if compared with the first algorithm for all the test cases considered in the present paper. For some cases, such as the supersonic flow over the forward-facing step, the third algorithm was unstable. The fourth algorithm, as the first one, has presented good results for the test cases analyzed here. Despite the fact that this algorithm is more costly than the first one, it presented less cells that needed to have their order of accuracy reduced. The WENO schemes implemented with this algorithm presented the best results for all test cases. The ENO schemes implemented with the fourth algorithm have presented the best results among the ENO schemes.

IV. Multigrid Scheme

In this section, a general discussion of the implementation of a full approximation storage multigrid algorithm [22] is presented. With the use of the multigrid procedure, the discretized problem for the fine mesh is solved in an approximate manner on coarser meshes. As the coarse meshes have fewer points than the initial fine mesh, the solution of the problem in the coarse meshes requires a lower computational cost than in the initial fine mesh. The properties of the fine mesh are transferred to the coarse meshes by restriction operators and subsequently, the solution in the fine mesh is updated by prolongation operators, which transfer the properties from the coarse meshes. The restriction operator used in the present work is the volume weighted average [23,24], where the restricted conserved properties for the fine mesh cells forming the coarse mesh volumes are equal to the sum of the conserved properties of all the fine mesh cells that compose the coarse mesh volumes weighted by their volumes. The prolongation operator implemented in the present work uses direct injection of the coarse mesh values into the fine mesh [23–25].

The multigrid scheme implemented in the present work is based upon an agglomeration procedure [23–25] for generating the coarse meshes. A "seed" volume is chosen in the fine mesh and then all the volumes that have a node or an edge in common with this seed volume are grouped and they form the coarse mesh volume. A

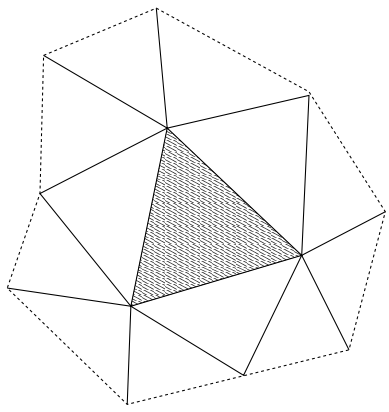

Fig. 9 Example for the agglomeration procedure with the seed volume (hatched volume).

schematic representation of the agglomeration procedure is shown in Fig. 9, where the hatched volume is the seed volume and the dashed line indicates the corresponding coarse mesh volume. Another seed volume is selected and the agglomeration procedure continues grouping all the fine mesh volumes. It should be noted that, during the agglomeration procedure, only the volumes that have not already been agglomerated may be grouped to form a coarse mesh volume. This is a necessary condition to guarantee that there is no volume overlapping in the coarse mesh. The selection of the seed volumes is not random to obtain a better coarse mesh quality. A list containing all the fine mesh volumes is generated before the agglomeration procedure and the volumes close to the boundaries are chosen to be first selected for the agglomeration. Further discussion of the agglomeration multigrid procedure here used can be found in [22].

V. Adaptive Mesh Refinement

In the present work, grid adaptation is used to improve the quality of the solution by increasing the number of grid points in regions where shock and expansion waves are present. Hence, a property sensor based on the solution obtained in the original mesh is computed and it is used to determine in which regions additional computational points are necessary. The general definition of the sensor, following the work in [1,2], can be expressed as

$$(\text{sensor})_i = \left\{ \max_m \left[\frac{|\psi_m|}{\psi_{m_{\max}} - \psi_{m_{\min}}} \right] \right\}_i \tag{40}$$

where ψ_m can be any conserved or primitive variable and $\psi_{m_{\max}}$ and $\psi_{m_{\min}}$ are the maximum and the minimum values of the ψ_m property in the flowfield. All volumes in which the sensor exceeds some specified threshold value are refined. Additional information about the implementation of the adaptive mesh refinement procedure can also be found in [1,2].

VI. Results

The present section discusses computational results for the second-order and third-order schemes, which were formulated for meshes composed by triangles and quadrilaterals. The objective of the present study is to verify the newly implemented capability and to assess its advantages/disadvantages with regard to the discretization methods previously available in the code. Hence, the test cases analyzed here were selected among those for which analytical solutions and/or well-documented, independent data are available in the literature.

A. Wedge Flow

The first case shown is the computation of the supersonic flowfield past a wedge with a half-angle $\theta = 10$ deg. For the present case, the multigrid method and the adaptive mesh refinement capability are used to accelerate the convergence rate and to have a better resolution of the shock wave that appears in the flow. The initial mesh, with

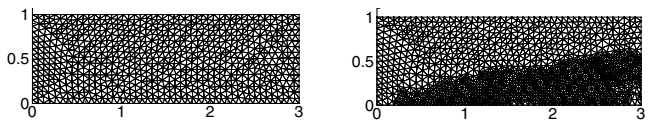

a) Coarse mesh **b) Refined mesh**

Fig. 10 Meshes used in the wedge flow simulation.

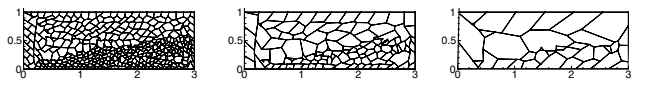

a) Mesh after the first agglomeration **b) Mesh after the second agglomeration** **c) Mesh after the third agglomeration**

Fig. 11 Coarse agglomerated meshes obtained from the grid shown in Fig. 10b.

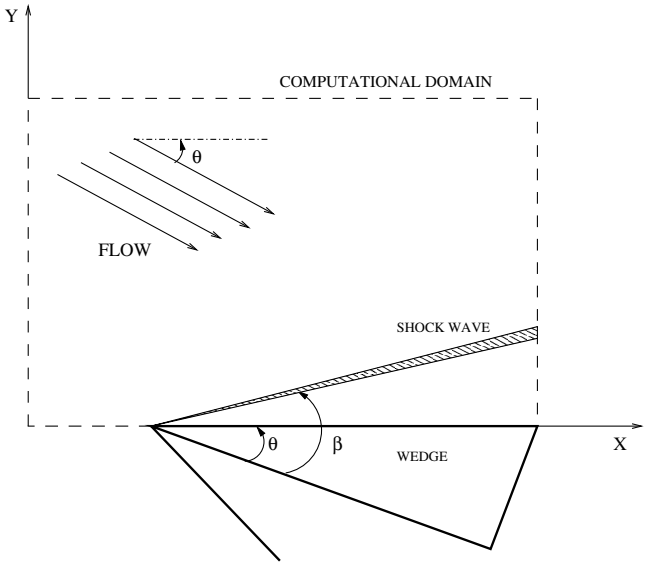

Fig. 12 Schematic representation of the computational domain.

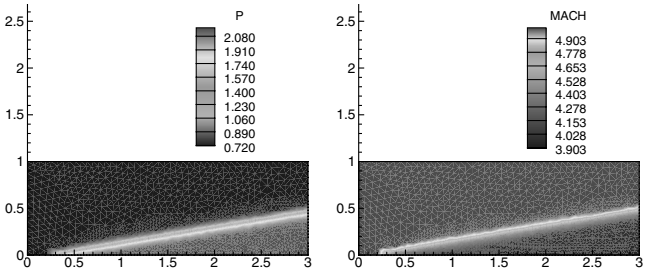

a) Pressure contours **b) Mach number contours**

Fig. 13 Results for the wedge flow simulation, $M_1 = 5.0$.

816 nodes and 1504 volumes, is shown in Fig. 10. The refined mesh, after one refinement pass, containing 1611 nodes and 3057 volumes, is also shown in Fig. 10. The coarse meshes used in the multigrid levels are shown in Fig. 11. One can see that three multigrid coarse mesh levels are used for the calculations in the case studied here. The leading edge of the wedge is located at coordinates x = 0.25 and y = 0.0. The computational domain is bounded along the bottom by the wedge surface and by an outflow section as represented in Fig. 12. Therefore, one has an inflow boundary located at the left and at the top of the domain, whereas the outflow boundary is located ahead of the wedge and at the right of the domain.

The well-known analytical solution for the present case gives the change in properties across the oblique shock as a function of the freestream Mach number and shock angle. The shock angle is known as an implicit function of the freestream Mach number and wedge half-angle (θ–β–Mach relation). The inviscid flow conditions on each side of the oblique shock are uniform. For the present case, the freestream Mach number was set as $M_1 = 5.0$ and, using the well-known analytical relations appearing in the literature [26], one can find an oblique shock with $\beta \approx 19.5$ deg. For the analytical solution, one has a pressure ratio of $p_2/p_1 \approx 3.083$ and a Mach number behind the shock wave of $M_2 \approx 3.939$. The numerical solutions are in good agreement with the analytical solutions, as can be seen in Fig. 13, and the values obtained in the computations are $p_2/p_1 \approx 3.048$ and $M_2 \approx 3.932$. The solution appearing in Fig. 13 is for a calculation with the second-order accurate WENO scheme using Roe's method [6] and the second-order TVD Runge–Kutta scheme for time integration. The results are obtained for the refined mesh presented in Fig. 10.

Tests were performed for the second-order ENO and WENO schemes with spatial discretizations considering Roe's flux-difference splitting [6] and Liou's AUSM+ flux-vector splitting

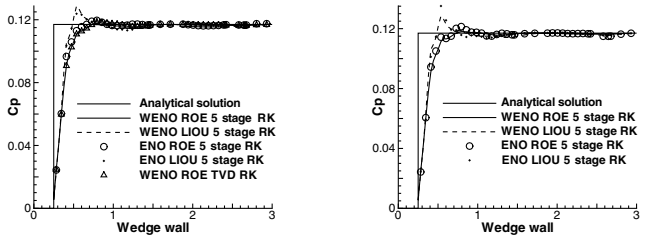

a) Results for the Jiang/Shu [20] oscillation indicator

b) Results for the Abgrall [17] oscillation indicator

Fig. 14 Cp distribution along the wedge wall, $M_1 = 5.0$.

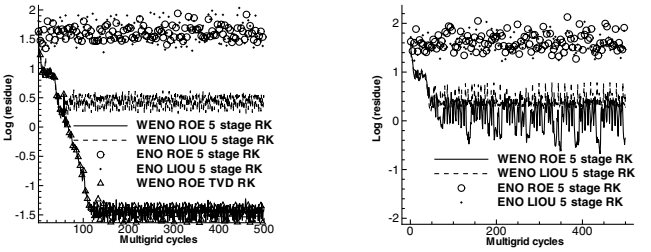

a) Residue for the Jiang/Shu [20] oscillation indicator

b) Residue for the Abgrall [17] oscillation indicator

Fig. 15 Residue histories for the wedge flow simulation, $M_1 = 5.0$.

methods [5], and for the five-stage Runge–Kutta and the two-stage TVD Runge–Kutta schemes. All the studied schemes presented similar solutions with regard to the shock position and to the flow properties. Both Runge–Kutta schemes presented similar results considering the convergence rate and the maximum allowable CFL number for stability, besides the fact that the TVD Runge–Kutta scheme uses less computational effort due to the reduced number of stages. The WENO schemes have shown a better convergence rate than the ENO schemes, as expected. However, the converged solutions obtained were similar. The expressive differences that appeared in the solutions occurred due to the different numerical flux functions implemented. The Roe scheme [6] has shown to be more accurate in capturing the shock wave than the Liou scheme [5]. This can be observed in Fig. 14, where the pressure coefficient Cp is plotted for the wedge surface. The Liou scheme presented an overshoot in the presence of the shock wave and the Roe scheme [6] captured it without any overshoots. The convergence rates for both numerical flux functions are shown in Fig. 15. One can see that Roe's scheme reached a lower value for the residue than Liou's scheme [5].

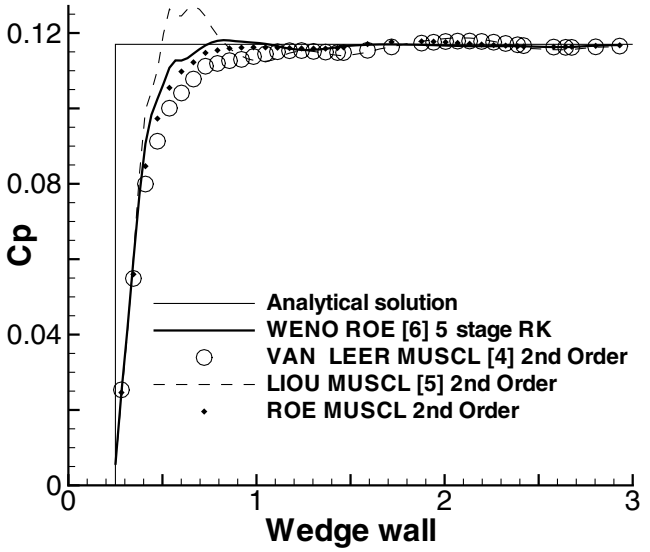

Fig. 16 Comparison among second-order schemes for the wedge flow, $M_1 = 5.0$.

Furthermore, one can also see that the ENO schemes do not present a significant decrease in residue value.

Different oscillation indicators were tested and the solution was compared for the Cp distribution along the wedge surface. One can see that the oscillation indicator proposed by Jiang and Shu [20] presented better results than the one proposed by Abgrall [17]. The solutions obtained with the former have not shown significant oscillations, whereas the solutions obtained with Abgrall's oscillation indicator have done so. In Fig. 14, the solutions for the different oscillation indicators for the ENO and WENO schemes with reconstructions considering Roe's [6] and Liou's [5] numerical flux functions are plotted. Results for the oscillation indicator proposed by Harten and Chakravarthy [19] are not shown due to the similarity of the formulation and solution with those of the one proposed by Jiang and Shu [20] for the second-order method.

In Fig. 16 one can see the comparison of the Cp distributions along the wedge wall for different second-order schemes. The results presented here are for the second-order WENO scheme, with Roe's [6] method for flux evaluation. These results are compared with flux-vector splitting calculations, using Liou's AUSM+ [5] and van Leer's [4] methods, and flux-difference splitting computations, using Roe's [6] method. All FVS and FDS numerical flux functions are implemented using MUSCL reconstruction and a multidimensional "minmod" [12] limiter. For the temporal discretization, all cases have used the five-stage Runge–Kutta scheme. The results show that oscillations appear in Liou's [5] scheme, that van Leer's [4] scheme is very diffusive, and that Roe's [6] scheme is the more accurate MUSCL method presented here. Furthermore, the results also show that the WENO scheme captured a more accurate solution, without oscillations and less diffusive when compared with the other methods.

B. Ringleb Flow

The second test case presents a study of the order of accuracy for the schemes analyzed here using the Ringleb flow problem [27]. The Ringleb flow is basically a potential flow in a strongly bent duct and can be described analytically. At any point in the domain, the flow is characterized by two parameters, q and k. The parameter q is the nondimensional velocity that is constant along isoline circles, and the parameter k is constant along the streamlines. The domain used in the present computations has taken the streamline with $k = 0.8$ and $k = 0.4$ for the inner and outer walls of the duct, respectively. The choice of these parameters guarantees that the flow is subsonic everywhere. The inlet and the outlet of the duct are chosen as being the velocity isoline $q = 0.3$ and the boundary conditions were set in agreement with [28]. An intermediate triangular mesh used in the present computations, the exact solution obtained in terms of density contours, and the numerical solution obtained with the third-order WENO scheme can be observed in Fig. 17.

For this test case, the order of accuracy of the ENO and WENO schemes is measured through the computation of the $L2$ norm of the error in the density distribution as a function of the mesh refinement. The solutions were carried out with the second-order ENO and

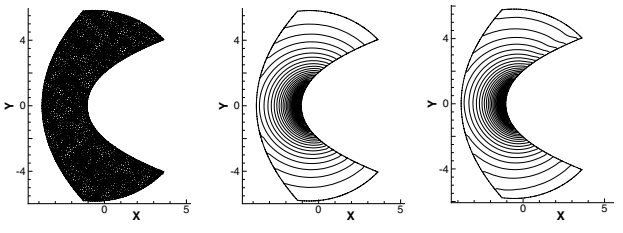

a) Intermediate mesh used in the Ringleb [27] flow computations

b) Density contour lines of the exact solution

c) Density contour lines for the numerical solution obtained with the third-order WENO method

Fig. 17 Computational grid and solutions for the Ringleb flow problem [27].

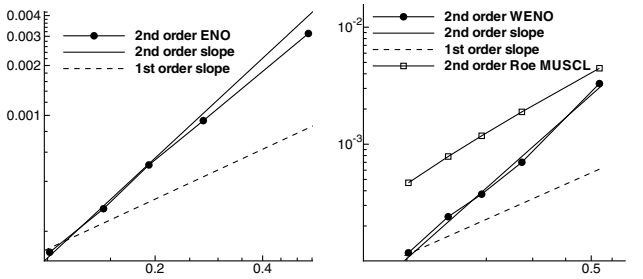

a) Results obtained for second-order ENO-Roe reconstruction [6]

b) Results obtained for second-order WENO-Roe reconstruction

Fig. 18 Discrete L2 norm of density error as a function of mesh width.

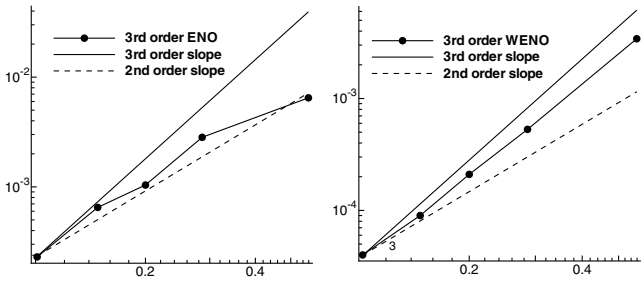

a) Results obtained for third-order ENO-Roe reconstruction [6]

b) Results obtained for third-order WENO-Roe reconstruction

Fig. 19 Discrete L2 norm of density error as a function of mesh width.

WENO schemes and the third-order ENO and WENO schemes using the Jiang and Shu [20] oscillation indicator. In Fig. 18, one can observe the results for the second-order ENO and WENO schemes and for the second-order MUSCL scheme. All the computations performed for this test case considered the Roe FDS method [6] for the numerical flux computation. The slopes that indicate ideal first- and second-order accuracy are also plotted with the aim of comparison with the order of accuracy of the schemes analyzed here. The slope of the best-fit, least-square line, through a plot of the logarithm of the $L2$ norm of the density error as a function of the logarithm of the mesh width, gives a measure of the true order of accuracy of the method. The results of such study are shown in Table 1 for all cases considered here. One can see that the second-order WENO scheme indeed achieves second-order accuracy, whereas the second-order ENO scheme also comes very close to achieving second-order accuracy. The MUSCL scheme plotted in Fig. 18 achieved the smallest order of accuracy among the methods analyzed here, as also indicated in Table 1. The third-order methods are shown in Fig. 19 together with the slopes that indicate ideal second- and third-order accuracy. One can observe in Table 1 that the third-order ENO scheme achieved only second-order accuracy, while the third-order WENO scheme presented the best results in terms of order of accuracy. The actual order of accuracy obtained with the third-order WENO scheme is 2.66, which is only slightly lower than the theoretical one.

Table 1 Order of accuracy for Ringleb flow computation [27]

Method	Order of accuracy
Second-order MUSCL	1.34
Second-order ENO	1.83
Second-order WENO	1.97
Third-order ENO	1.96
Third-order WENO	2.66

The results for the third-order schemes are directly related to the reconstructions close to the boundaries. In such regions, the algorithm for stencil selection does not have sufficient neighbors to reconstruct a third-order scheme and the order of accuracy decreases to second-order. The second-order schemes and the third-order ENO scheme presented similar results, in terms of order of accuracy, which is in agreement with the results shown in [11]. Therefore, as usually mentioned in the literature, the present results also indicate that the WENO schemes have a higher order of accuracy than their corresponding ENO schemes.

C. Shock Tube Problem

The third test case analyzed is a shock tube problem with length 10.0 and height 1.0, in dimensionless units, discretized with a mesh containing 4697 nodes and 8928 triangular control volumes. The entire mesh and a detailed part of it are shown in Fig. 20. The results presented here are for a pressure ratio, $p_1/p_4 = 5.0$. Here, p_1 denotes the initial static pressure in the driver section (high-pressure side) of the shock tube, whereas p_4 denotes the corresponding initial static pressure in the driven section (low-pressure side) of the shock tube. The dimensionless pressure in the driver section was set to $p_1 = 0.8571$. Density was made dimensionless with respect to the initial density, and pressure was made dimensionless with respect to the density times the speed of sound squared, both with respect to the driver section of the shock tube. It was assumed that both sides of the shock tube were originally at the same temperature.

Figure 21 presents the results for the flow in the shock tube for an instant of time equal to 1.0 dimensionless time units after diaphragm rupture. The results are presented in terms of density distribution along the shock tube centerline. The results are plotted for the second-order WENO scheme, for the third-order ENO and WENO schemes, and for the van Leer [4] flux-vector splitting MUSCL scheme with a multidimensional minmod limiter. All WENO schemes and the ENO scheme used Roe's [6] spatial discretization and the oscillation indicator proposed by Jiang and Shu [20]. The second-order schemes used the second-order TVD Runge–Kutta

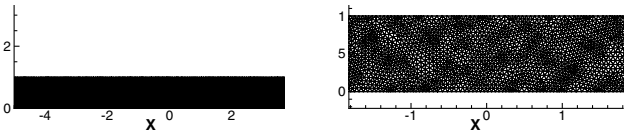

a) Entire mesh for the shock tube problem

b) Detail of the mesh for the shock tube problem

Fig. 20 Shock tube mesh.

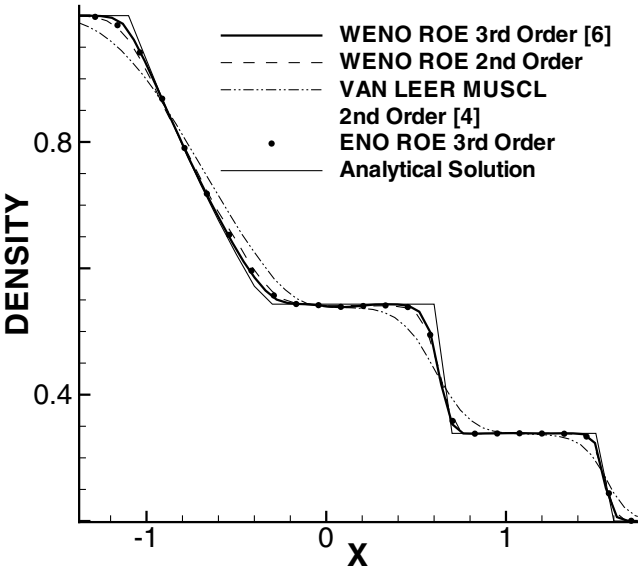

Fig. 21 Density along the centerline of the shock tube.

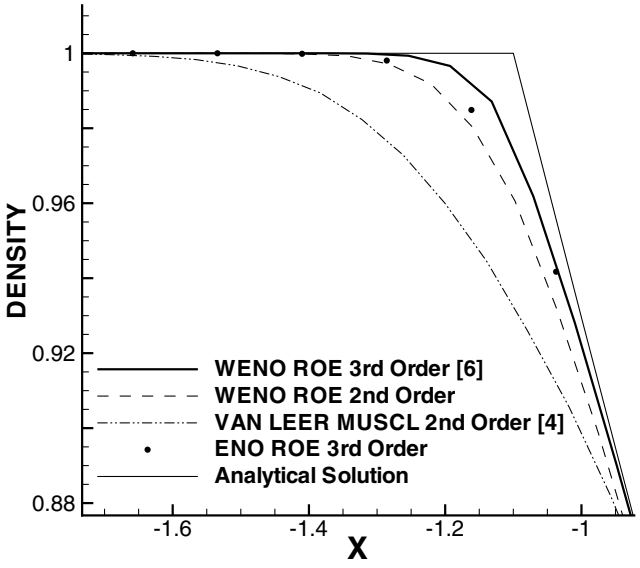

a) Detail of the expansion wave region

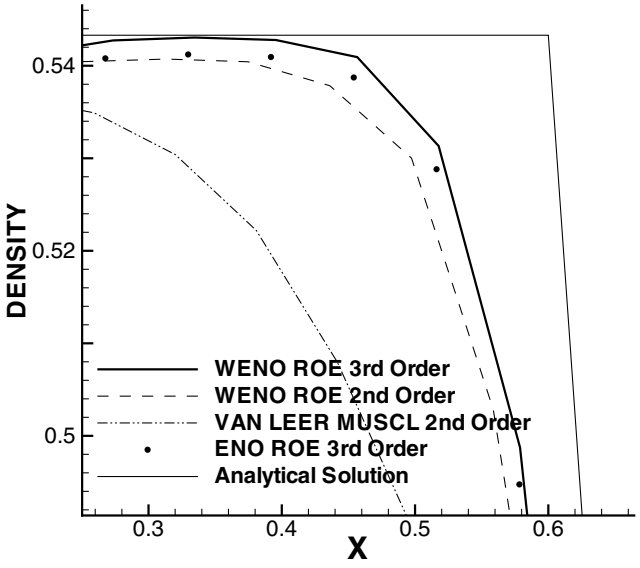

b) Detail of the contact discontinuity region

Fig. 22 Enlarged view of density along the centerline of the shock tube.

temporal discretization and the third-order schemes used the third-order TVD Runge–Kutta temporal discretization. The analytical solution is also plotted with the purpose of comparing the quality of the numerical solutions.

In this problem, a normal shock wave moves from the driver section of the shock tube to the driven section. As the normal shock wave propagates to the right with some speed, it increases the pressure and induces a mass motion of the gas behind it. The interface between the driver and driven gasses is represented by a contact discontinuity. An expansion wave propagates to the left, smoothly and continuously decreasing the pressure in the driver section of the shock tube. All these physical phenomena are well captured by ENO and WENO schemes of second- and third-order of accuracy, as can be viewed in Fig. 21.

The ENO and WENO schemes are less diffusive than the van Leer [4] scheme. Such a conclusion can be readily reached by observing the sharper representation of the shock wave and the contact discontinuity. One can see in the results that the third-order accurate schemes provided a sharper representation of the expansion wave and the contact discontinuity. The results also show that the third-order WENO scheme is more accurate than the third-order ENO scheme. This can be seen in Fig. 22, where one can clearly observe that the first scheme yields a sharper representation of the expansion wave and the contact discontinuity.

D. Forward-Facing Step

The fourth test case is a compressible flow in a channel with a forward-facing step that is well documented in [29]. The channel length is 3, with height 1, in dimensionless units. The step is located in a position with 0.6 dimensionless units from the channel entrance. It has a height of 0.2 dimensionless units. Three different meshes are used to test the schemes. The first mesh considered in this test case has 16,384 nodes and 16,064 quadrilateral control volumes. A blown-up view of the step region can be seen in Fig. 23. The second and third meshes considered in this test case are composed exclusively by triangular control volumes and have 7022 and 13,256 nodes, and 13,608 and 25,850 control volumes, respectively. The blown-up view of the step region for both meshes can be seen in Fig. 24 for the coarser mesh and in Fig. 25 for the finer mesh. A uniform Mach number of 3.0 is set as inflow at $t = 0$ dimensionless time units. Density was made dimensionless with respect to the entrance condition and pressure was made dimensionless with

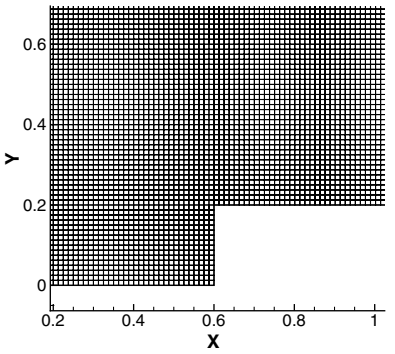

Fig. 23 Detail of the step corner region for the quadrilateral mesh.

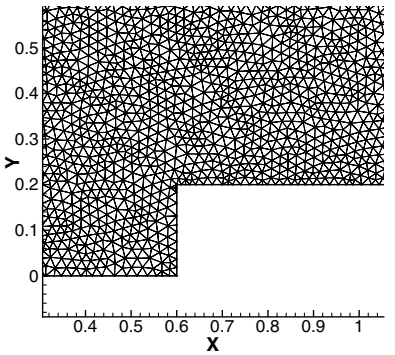

Fig. 24 Detail of the step corner region for the coarse triangular mesh.

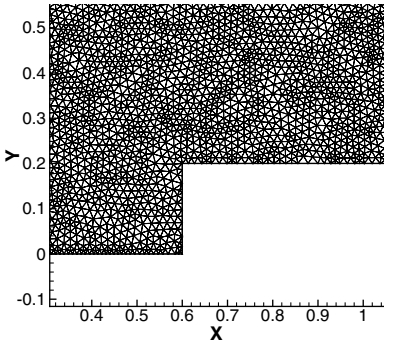

Fig. 25 Detail of the step corner region for the fine triangular mesh.

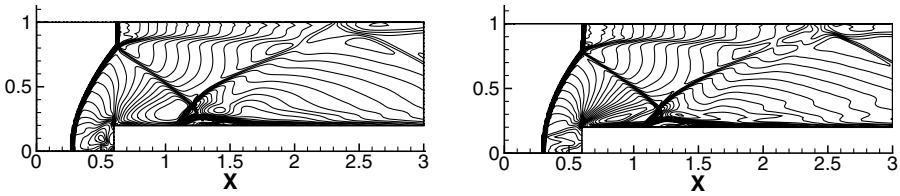

a) Mach number contours for the second-order WENO scheme

b) Mach number contours for the third-order WENO scheme

Fig. 26 Mach number contours at $t = 4.0$ dimensionless time units for the mesh in Fig. 23.

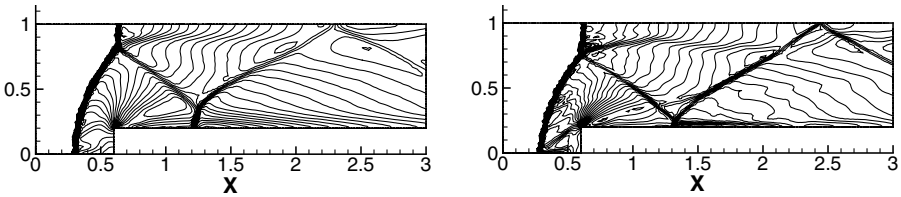

a) Mach number contours for the second-order WENO scheme

b) Mach number contours for the third-order WENO scheme

Fig. 27 Mach number contours at $t = 4.0$ dimensionless time units for the mesh in Fig. 24.

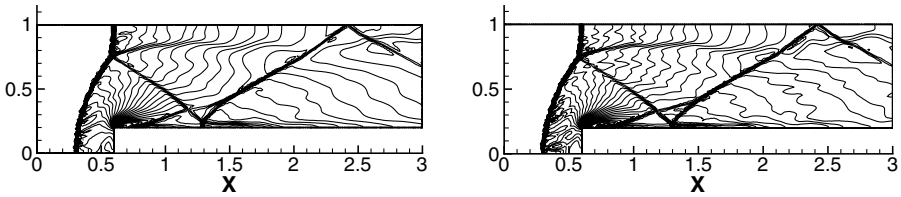

a) Mach number contours for the second-order WENO scheme

b) Mach number contours for the third-order WENO scheme

Fig. 28 Mach number contours at $t = 4.0$ dimensionless time units for the mesh in Fig. 25.

respect to the density times the speed of sound squared. One should observe that this test case considers unsteady flow.

The more interesting structure of the flow develops at time equal to $t = 4.0$ dimensionless time units. Results at this instant of time appear in Figs. 26–28 for the computation with WENO schemes. In Fig. 26a, one can see the solution for the second-order WENO scheme, and in Fig. 26b one can see the solution for the third-order WENO scheme. The solutions presented in Figs. 26a and 26b are obtained for the mesh composed exclusively by quadrilateral control volumes. In Figs. 27a and 28a, one can see the solutions for the second-order WENO scheme, and in Figs. 27b and 28b one can see the solutions for the third-order WENO scheme. The solutions presented in Fig. 27 are obtained for the triangular coarser mesh and the solutions in Fig. 28 are obtained for the triangular finer mesh. The second-order WENO scheme analyzed in this test case uses the second-order TVD Runge–Kutta scheme and the third-order WENO scheme uses the third-order TVD Runge–Kutta scheme for the time march. Roe's [6] numerical flux function is used to evaluate the flux in the edges of the control volumes for all the schemes. All solutions presented for this test case for the third-order WENO scheme use the first algorithm for stencil selection, as discussed in preceding sections.

At the instant of time presented in the solutions, a detached shock evolves to a lambda shock that reflects in the upper channel wall. A contact discontinuity is created past the lambda shock and both the reflected shock and the contact discontinuity move downstream along the channel. The reflected shock is again reflected at the lower wall, as well as at the upper wall near the end of the channel. The contact discontinuity interacts with the shock that reflects in the lower wall. This interaction occurs in the region near the end of the channel, just upstream of the last shock reflection. At the corner region, there is also a weak oblique shock wave that ends the expansion region due to a Prandtl–Meyer expansion fan. This weak shock interacts with the first reflected shock near the lower wall of the channel. This leads typically to a flow structure that resembles a nonphysical shock-boundary layer interaction in the region where the second shock reflection occurs. The solution in this region is very dependent on the treatment applied to the corner of the step. In the present work, no special treatment was applied to the corner of the step, contrary to the procedure adopted in the original reference [29]. One can see that the results presented here are similar to those presented in [10,17], where, as in this work, no special treatment was applied to the corner of the step.

The results obtained in Fig. 26 for the mesh composed by quadrilateral control volumes present a very sharp capture of the first detached shock and of the lambda shock that reflects on the upper wall of the channel. The contact discontinuity was also well captured for both second- and third-order WENO schemes. The first shock reflection, as well as the second reflection, were well defined in the solutions for both schemes. For the mesh in Fig. 23, one can observe that the second reflection of the shock, which occurs in the lower wall, was affected by the nonphysical shock-boundary layer interaction created downstream of the corner region. This shock-boundary layer interaction is very pronounced for both solutions obtained with the WENO schemes and the quadrilateral mesh. One can see that the third-order WENO scheme captured the expansion fan as well as the weak compression shock near the corner region. The second-order WENO scheme was not able to capture such phenomena. In the postshock region, in the lower wall of the channel, one can observe a separation bubble. This circulation zone appears only for the calculations with the quadrilateral mesh. The region where the contact discontinuity and the second shock reflection meet and the third reflection of the shock, near the end of the channel, are better resolved by the third-order WENO scheme.

The results obtained for the coarse mesh composed by triangular control volumes presented a difference regarding the height of the lambda shock position. One can see that the lambda shock forms closer to the wall for the second-order WENO scheme and this affects

the position of the contact discontinuity. In Fig. 27, one can see that all the shock reflections and the contact discontinuity are better captured for the third-order scheme. The second-order WENO scheme presents the shock-boundary layer interaction created past the corner region in the lower wall of the channel, although such effect is much less pronounced in this case than in the solutions with the quadrilateral meshes. In other words, the second reflection of the shock presents a Y-shock instead of a simple reflection in the wall. The results for the second-order scheme in the region where the interaction between the contact discontinuity and the last shock reflection occurs are poor in comparison with the third-order scheme results. The third-order WENO scheme captures the weak shock near the corner region well, as in the results shown in Sonar [10]. This scheme indicates a much less pronounced shock-boundary layer interaction-type phenomenon in the second shock reflection in the lower wall of the channel. All the shock reflections have a better resolution for the third-order WENO scheme and they are in the correct positions when compared with [29].

The results obtained for the fine triangular mesh present the more accurate capture of the flow features for this test case, as one can see in Fig. 28. All the flow features were more sharply captured due to the mesh refinement. For this finer mesh, the second-order WENO scheme has captured the contact discontinuity and the shock wave generated in the corner of the step, different from the result in the coarse triangular mesh. However, the third-order scheme presented more accurate results than the second-order scheme. For the third-order scheme, the shock wave reflections and the contact discontinuity are sharper than for the second-order scheme. One can observe that the nonphysical shock-boundary layer interaction has almost disappeared for the second-order scheme and has completely disappeared for the third-order scheme solutions. This fact is related to the mesh refinement and to the order of accuracy of the schemes. A refined mesh and a higher order scheme tends to diminish the appearance of the nonphysical shock-boundary layer interaction. The correct capture of the shock wave created at the corner of the step can be seen only for the triangular finer mesh. Hence, it is clear that the appearance of the nonphysical shock-boundary layer interaction along the lower wall is directly related to the resolution of the corner flow, and the solution can always be improved with adequate mesh refinement.

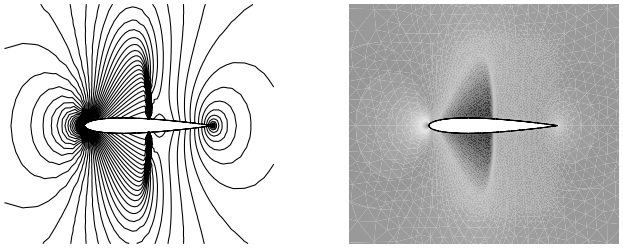

a) Pressure contour lines over the NACA0012 airfoil in transonic flow

b) Pressure contours over the NACA0012 airfoil in transonic flow

Fig. 30 Transonic flow over a NACA 0012 airfoil, $M_\infty = 0.8$ and AOA = 0.

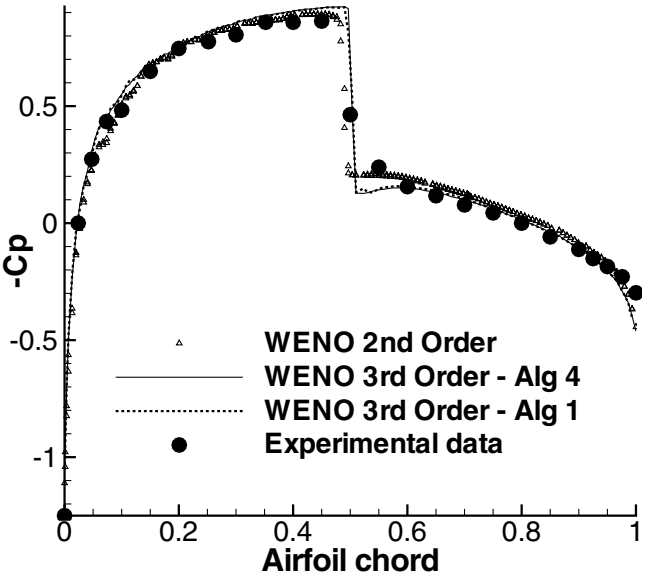

Fig. 31 Cp distributions for a NACA 0012 airfoil, $M_\infty = 0.8$ and AOA = 0.

E. NACA 0012 Airfoil

The fifth test case considered here is the transonic flow over a NACA 0012 airfoil with zero degree angle-of-attack. The freestream has a Mach number value of $M_\infty = 0.8$. Density is made dimensionless with respect to the freestream condition and pressure is made dimensionless with respect to the density times the speed of sound squared. This case is computed using an unstructured mesh with 4369 nodes and 8414 triangular control volumes. Two additional agglomerated grids are used in the multigrid computations for this case and one can see a detail of the fine mesh and of the agglomerated meshes in Fig. 29. This is a steady case and, hence, the CFL number is set as a constant value. Therefore, different from the previous unsteady computations in which the time step is set constant throughout the flowfield, the CFL number is kept constant throughout the flow in the present steady computation. Hence, one sets the CFL number and the local time step is computed using the local grid spacing and characteristic speeds. The numerical results for the pressure contours are plotted in Fig. 30 for the third-order WENO scheme computed with the first algorithm for stencil selection. For this case, both the ENO and the WENO schemes present similar converged results for the third-order schemes. However, the WENO schemes present a better convergence rate. The Cp distributions along the airfoil chord obtained with the second-order WENO scheme, the third-order WENO schemes implemented using the first and fourth stencil selection algorithms, and for the experimental data obtained from [30] are plotted in Fig. 31. The computations with the spatially second-order method use the second-order TVD Runge–Kutta scheme for the temporal discretization, whereas those with the spatially third-order methods used the third-order TVD Runge–Kutta scheme. All schemes considered Roe's [6] method for numerical flux evaluation.

Figure 31 indicates that the third-order methods do a better job of capturing the shock wave over the airfoil, if compared with the second-order method. Moreover, there are oscillations in the leading-edge region of the airfoil for the second-order solution, which vanish for both third-order algorithms tested in this case. The sharper definition of the shock wave, obtained with the third-order methods, is further emphasized by the reduced number of cells within the shock. The Cp distributions in the post-shock region again confirm the better resolution obtained with the third-order schemes. A comparison of the third-order scheme results also indicates that the calculations using the fourth algorithm for stencil selection yielded a Cp distribution without overshoots in the postshock region, whereas

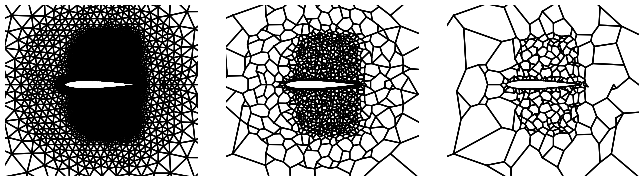

a) Mesh over the NACA0012

b) Mesh after the first agglomeration pass

c) Mesh after the second agglomeration pass

Fig. 29 Detail of the meshes used in the simulation of the transonic flow over a NACA0012.

the use of the first algorithm led to a slight overshoot immediately downstream of the shock. Furthermore, the former yielded a solution with only one cell inside the shock structure. Finally, it is important to emphasize that the present computations are performed assuming inviscid flow. Nevertheless, the computational results are in good agreement with the available experimental data. One should observe, however, that the pressure rise across the shock wave, in the experimental results, is spread over a larger region due to the presence of the boundary layer and the consequent shock-boundary layer interaction that necessarily occurs in the experiment. For the numerical solution, the shock presents a sharper resolution, as one can expect for an Euler calculation.

F. Royal Aerospace Establishment 2822 Airfoil

The last test case considered here is the transonic flow over a Royal Aircraft Establishment (RAE) 2822 airfoil with 2.31 deg angle-of-attack. The freestream has a Mach number value of $M_\infty = 0.729$. Density is made dimensionless with respect to the freestream condition and pressure is made dimensionless with respect to the density times the speed of sound squared. This case is computed using a mesh with 5435 nodes and 10,260 triangular control volumes. Two additional agglomerated grids are used in the computations for this case and one can see a detail of the fine mesh and of the agglomerated multigrid meshes in Fig. 32. As in the flowfield computation for the NACA 0012 airfoil, this is a steady case and, hence, the CFL number is set at a constant value. For this case, only the WENO schemes present results in agreement with the correct physics of the flow. The ENO schemes did not present satisfactory results for meshes composed exclusively by triangles. However, for meshes composed exclusively by quadrilaterals, the ENO schemes present solutions in agreement with the physics of the flow for this test case. Further studies must be performed for the ENO schemes to reach a full understanding of the method behavior for triangular grids. The numerical results in terms of pressure contours are plotted in Fig. 33 for the third-order WENO scheme computed with the first algorithm for stencil selection, and using the triangular grid shown in Fig. 32. One can see a comparison of the residue histories for the third-order WENO schemes used in this simulation in Fig. 34. One can observe that the convergence rate is directly related to the number of stencils used in the reconstructions. A larger number of stencils provides an improved convergence rate as can be seen in Fig. 34.

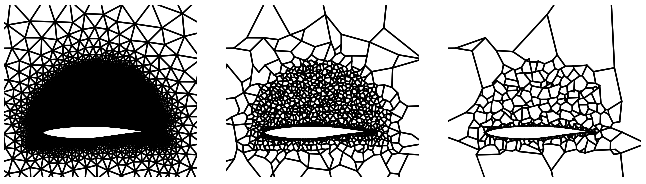

a) Mesh over the RAE2822 b) Mesh after the first agglomeration pass c) Mesh after the second agglomeration pass

Fig. 32 Detail of the meshes used in the simulation over a RAE 2822 airfoil.

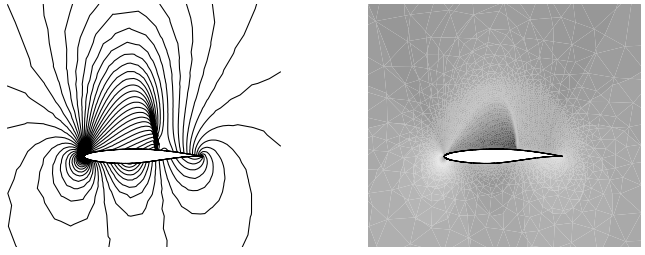

a) Pressure contour lines over the RAE2822 airfoil in transonic flow b) Pressure contours over the RAE2822 air-foil in transonic flow

Fig. 33 Transonic flow over a RAE 2822 airfoil, $M_\infty = 0.729$ and AOA = 2.31 deg.

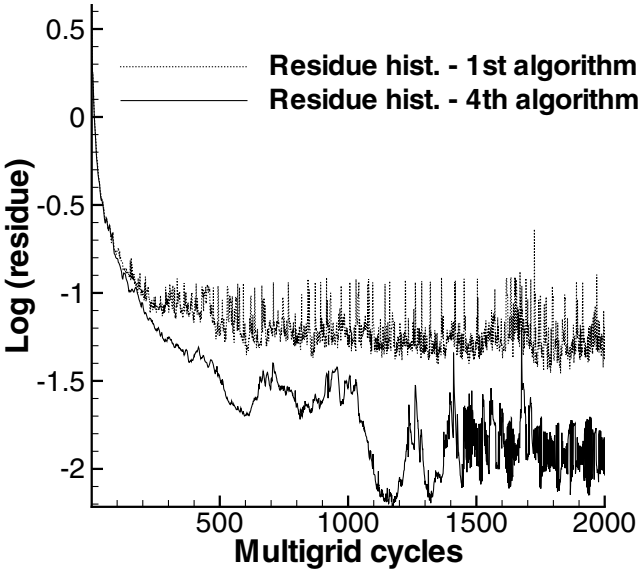

Fig. 34 Residue histories for third-order WENO algorithms, transonic flow over RAE 2822 airfoil.

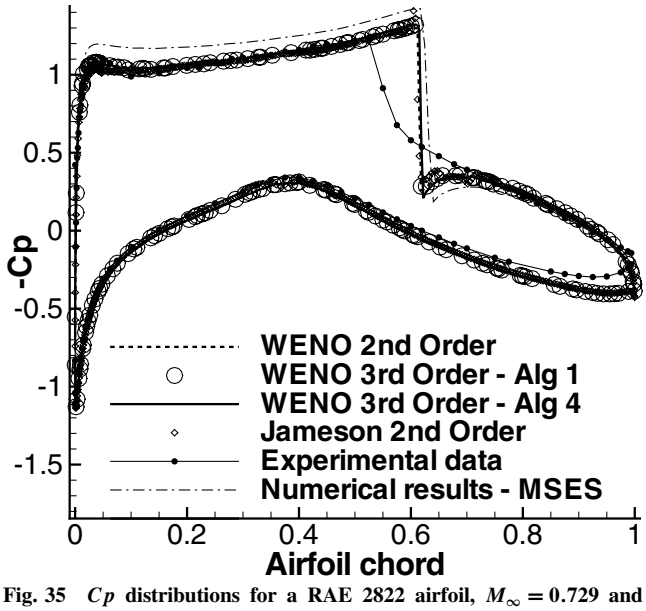

Fig. 35 Cp distributions for a RAE 2822 airfoil, $M_\infty = 0.729$ and AOA = 2.31 deg.

The Cp distributions along the airfoil chord are plotted in Fig. 35. The results are obtained using the second-order Jameson scheme already validated in the code [1,22], the second-order WENO scheme, the third-order WENO schemes implemented using the first and fourth algorithms for stencil selection, the experimental data obtained from [30], the numerical solution obtained with the MSES software [31], and the experimental data obtained from [32]. The spatially second-order methods use the second-order five-stage Runge–Kutta scheme for the temporal discretization while the spatially third-order methods use the third-order TVD Runge–Kutta scheme. All the WENO schemes considered Roe's method in the spatial discretization. Despite the fact that the present computations are for inviscid flow, the results are in good agreement with the

experimental data presented. One can see that, in the experimental data, the shock wave moves upstream over the airfoil due to the boundary layer presence. In the trailing edge of the airfoil, the viscous effects are again visible in the solution. One can observe the better resolution of the WENO methods, if compared with Jameson's method, in capturing the shock over the airfoil. The centered scheme presents overshoots upstream and downstream the shock. Both the second- and third-order WENO schemes capture the shock with a smaller number of cells inside the shock, i.e., they capture the shock with a sharper definition. The second-order WENO scheme does not capture the leading-edge Cp distribution as well as the other methods compared here. Although the numerical results obtained with the MSES code presented a lower Cp plateau in the region upstream the shock, the lower surface of the airfoil and the trailing-edge region are in agreement with the WENO results compared here. There is also a small difference in the shock resolution between the third-order WENO schemes using the first and the fourth algorithms for stencil selection. The fourth algorithm reached a higher value of Cp in the region immediately downstream the shock, similar to the MSES result. Therefore, as observed in a preceding section of this paper, the availability of more interpolation stencils, provided by the fourth algorithm, leads to an improved resolution of flow features.

VII. Conclusions

The reconstruction of essentially nonoscillatory schemes and weighted essentially nonoscillatory schemes is presented in this work. Different approaches for stencil selection are discussed for second- and third-order ENO and WENO schemes. Although, in this paper, only second- and third-order accurate schemes are actually implemented and assessed, the formulation of ENO and WENO reconstruction is treated in a generic framework that allows the construction of polynomials of any order and, hence, of schemes with an arbitrary order of accuracy. Details with regard to oscillation indicators are also treated. The Roe flux-difference splitting scheme [6] and the Liou flux-vector splitting scheme [5] are tested and compared in the paper, and different Runge–Kutta time marching schemes are implemented with similar purposes of comparison. A multigrid method is used for faster convergence to steady-state solutions. An adaptive refinement technique is also employed to yield a sharper representation of the strong gradients appearing in the flows.

The test cases studied in this work include the supersonic flow over a wedge, the Ringleb flow problem [27], a shock tube problem, the unsteady supersonic flow in a channel with a forward-facing step, the transonic flow over the NACA 0012 airfoil, and the transonic flow over the RAE 2822 airfoil. All of these test cases have their results compared with data available in the literature. The third-order schemes yield results with better resolution than the second-order schemes, and WENO schemes present better results in comparison to their corresponding ENO schemes. For the supersonic flow over a wedge, results show that oscillations appear in Liou's scheme [5], that van Leer's scheme [4] is very diffusive, and that Roe's scheme [6] is the more accurate MUSCL method compared here. Furthermore, the results also show that the WENO scheme captured a more accurate solution, without oscillations and less diffusive when compared with the other methods.

The analysis of the effective order of accuracy of the schemes is presented for the computation of the Ringleb flow problem [27]. The second-order schemes actually achieved their nominal order of accuracy. The third-order WENO scheme was able to obtain an actual of order of accuracy of 2.66, which is fairly close to the nominal one. The third-order ENO scheme only reached second-order accuracy, which is consistent with other results reported in the literature. These results are strongly related to the reconstructions close to the boundary regions.

One can see in the results for the shock tube problem that the ENO and WENO schemes provide a sharper representation of the flow features than the van Leer [4] flux-vector splitting scheme with MUSCL reconstruction. The results also show that the third-order WENO scheme is more accurate than the third-order ENO scheme. Moreover, the third-order schemes are more accurate than their corresponding second-order ones. The results for the quadrilateral mesh obtained for the forward-facing step flow show a nonphysical shock-boundary layer interaction created downstream of the corner region. The third-order WENO scheme does not present any shock-boundary layer interaction-type phenomenon for the fine triangular mesh. For the flows around the NACA 0012 and the RAE 2822 airfoils, one can observe that the availability of more interpolation stencils, provided by the third-order scheme with the fourth algorithm for stencil selection, leads to an improved resolution of flow features.

Acknowledgments

The authors gratefully acknowledge the support of Fundação de Amparo à Pesquisa do Estado de São Paulo through a Masters Scholarship for the first author under the Fundação de Amparo à Pesquisa do Estado de São Paulo Grant No. 03/10047-2. The authors also acknowledge the partial support of Conselho Nacional de Desenvolvimento Científico e Tecnológico under the Integrated Project Research Grant No. 501200/2003-7. The authors are also thankful to Edson Basso for the very fruitful discussions during the course of the present research.

References

[1] Azevedo, J. L. F., and Korzenowski, H., "Comparison of Unstructured Grid Finite Volume Methods for Cold Gas Hypersonic Flow Simulations," *Proceedings of the 16th AIAA Applied Aerodynamics Conference*, AIAA Paper 98-2629, June 1998, pp. 447–463.

[2] Figueira da Silva, L. F., Azevedo, J. L. F., and Korzenowski, H., "Unstructured Adaptive Grid Flow Simulations of Inert and Reactive Gas Mixtures," *Journal of Computational Physics*, Vol. 160, No. 2, May 2000, pp. 522–540.

[3] Azevedo, J. L. F., Figueira da Silva, L. F., and Strauss, D., "Order of Accuracy Study of Unstructured Grid Finite Volume Upwind Schemes," *Journal of the Brazilian Society of Mechanical Sciences and Engineering*, (submitted for publication).

[4] van Leer, B., "Flux-Vector Splitting for the Euler Equations," *Proceedings of the 8th International Conference on Numerical Methods in Fluid Dynamics, Lecture Notes in Physics*, Vol. 170, Springer-Verlag, Berlin, June 1982, pp. 507–512.

[5] Liou, M. S., "A Sequel to AUSM: AUSM+," *Journal of Computational Physics*, Vol. 129, No. 2, Dec. 1996, pp. 364–382.

[6] Roe, P. L., "Approximatte Riemann Solvers, Parameter Vectors, and Difference Schemes," *Journal of Computational Physics*, Vol. 43, No. 2, Oct. 1981, pp. 200–212.

[7] Anderson, W. K., Thomas, J. L., and van Leer, B., "A Comparison of Finite Volume Flux Vector Splittings for the Euler Equations," *AIAA Journal*, Vol. 24, No. 9, Sept. 1986, pp. 1453–1460.

[8] Harten, A., Osher, S., Engquist, B., and Chakravarthy, S. R., "Uniformly High-Order Accurate Essentially Non-Oscillatory Schemes 3," *Journal of Computational Physics*, Vol. 71, No. 2, Aug. 1987, pp. 231–303.

[9] Liu, X. D., Osher, S., and Chan, T., "Weighted Essentially Non-Oscillatory Schemes," *Journal of Computational Physics*, Vol. 115, No. 1, Nov. 1994, pp. 200–212.

[10] Sonar, T., "On the Construction of Essentially Non-Oscillatory Finite Volume Approximations to Hyperbolic Conservation Laws on General Triangulations: Polynomial Recovery, Accuracy and Stencil Selection," *Computer Methods in Applied Mechanics and Engineering*, Vol. 140, No. 2, Jan. 1997, pp. 157–181.

[11] Friedrich, O., "Weighted Essentially Non-Oscillatory Schemes for the Interpolation of Mean Values on Unstructured Grids," *Journal of Computational Physics*, Vol. 144, No. 1, July 1998, pp. 194–212.

[12] Hirsch, C., *Numerical Computation of Internal and External Flows*, Vol. 2, Wiley, New York, 1990.

[13] Liou, M. S., "A Continuing Search for a Near-Perfect Numerical Flux Scheme., Part 1: AUSM+," NASA TM-106524, NASA Lewis Research Center, Cleveland, OH, March 1994.

[14] Mavriplis, D. J., "Multigrid Solution of the Two Dimensional Euler Equations on Unstructured Triangular Meshes," *AIAA Journal*, Vol. 26, No. 7, July 1988, pp. 824–831.

[15] Shu, C. W., and Osher, S., "Efficient Implementation of Essentially Non-Oscillatory Shock-Capturing Schemes," *Journal of Computational Physics*, Vol. 77, No. 2, Aug. 1988, pp. 439–471.

[16] Gooch, C. F. O., "High Order ENO Schemes for Unstructured Meshes Based on Least-Squares Reconstruction," Argonne National Lab., Rept. P631-1296, Mathematics and Computer Science Div., Argonne National Lab., 1997.
[17] Abgrall, R., "On Essentially Non-Oscillatory Schemes on Unstructured Meshes: Analysis and Implementation," *Journal of Computational Physics*, Vol. 114, No. 1, Sept. 1994, pp. 45–58.
[18] Hu, C., and Shu, C. W., "Weighted Essentially Non-Oscillatory Schemes on Triangular Meshes," *Journal of Computational Physics*, Vol. 150, No. 1, March 1999, pp. 97–127.
[19] Harten, A., and Chakravarthy, S. R., "Multi-Dimensional ENO Schemes for General Geometries," Inst. for Computer Applications in Science and Engineering, Rept. 91-76, NASA Langley Research Center, 1991.
[20] Jiang, G. S., and Shu, C. W., "Efficient Implementation of Weighted ENO Schemes," *Journal of Computational Physics*, Vol. 126, No. 1, June 1996, pp. 77–99.
[21] Käser, M., and Iske, A., "ADER Schemes on Adaptive Triangular Meshes for Scalar Conservation Laws," *Journal of Computational Physics*, Vol. 205, No. 2, May 2005, pp. 486–508.
[22] Strauss, D., "An Unstructured Grid Approach to the Solution of Axisymmetric Launch Vehicle Flows," M.S. Thesis, Instituto Tecnológico de Aeronáutica, São José dos Campos, São Paulo, Brazil, Nov. 2001.
[23] Mavriplis, D. J., and Venkatakrishnan, V., "Agglomeration Multigrid for Viscous Turbulent Flows," *25th AIAA Fluid Dynamics Conference*, AIAA Paper 94-2332, June 1994, pp. 447–463.
[24] Sorensen, K. A., Hassan, O., Morgan, K., and Weatherill, N. P., "An Agglomeration Multigrid Method on Unstructured Hybrid Grids for Turbulent Compressible Flow," *Proceedings of the Conference of the European Community on Computational Methods in Applied Sciences* [CD-ROM], ECCOMAS, Barcelona, Spain, Sept. 2000.
[25] Venkatakrishnan, V., and Mavriplis, D. J., "Agglomeration Multigrid for the Three-Dimensional Euler Equations," *AIAA Journal*, Vol. 33, No. 4, 1995, pp. 633–640.
[26] Anderson, J. D., *Modern Compressible Flow*, McGraw–Hill, New York, 1982.
[27] Shapiro, A. H., *The Dynamics and Thermodynamics of Compressible Fluid Flow*, Vol. 2, Ronald, New York, 1954.
[28] Vankeirsbilck, P., and Deconinck, H., "Higher Order Upwind Finite Volume Schemes with ENO-properties for General Unstructured Meshes," AGARD Rept. 787, 1992.
[29] Woodward, P., and Colella, P., "The Numerical Simulation of Two-Dimensional Fluid Flow with Strong Shocks," *Journal of Computational Physics*, Vol. 54, No. 1, April 1984, pp. 115–173.
[30] Scalabrin, L. C., "Numerical Simulation of Three-Dimensional Flows Over Aerospace Configurations," M.S. Thesis, Instituto Tecnológico de Aeronáutica, São José dos Campos, São Paulo, Brazil, July 2002.
[31] Drela, M., "A User Guide to MSES 2.92," MIT Computational Aerospace Sciences Lab., Massachusetts Inst. of Technology, Dept. of Aeronautics and Astronautics, Cambridge, MA, 1996.
[32] NASA–NPARC Alliance CFD Verification and Validation Web Site, http://www.grc.nasa.gov/WWW/wind/valid/raetaf/raetaf01/raetaf01.html.

D. Gaitonde
Associate Editor